



**Politecnico  
di Torino**

**Politecnico di Torino**

Corso di Laurea Magistrale in Physics of Complex Systems

A.A. 2021/2022

Sessione di Laurea Novembre/Dicembre 2022

**Pressure waves propagation  
in hydraulic networks**

Relatore: Prof. Luca Ridolfi

Candidato: Elia Altimani

Correlatore: Prof. Riccardo Vesipa

Matricola: s272595

# Contents

|  |           |
|--|-----------|
| <b>INTRODUCTION</b>  | <b>1</b>  |
| <b>1 WATERHAMMER</b>   | <b>2</b>  |
| 1.1 Brief hystory . . . . .  | 2         |
| 1.2 Description of the phenomenon . . . . .  | 4         |
| 1.2.1 Velocity and pressure waves . . . . .  | 4         |
| 1.2.2 The four phases . . . . .  | 5         |
| 1.3 Equations of motion . . . . .  | 8         |
| 1.3.1 Dynamic equation . . . . .   | 8         |
| 1.3.2 Continuity equation . . . . .  | 10        |
| <b>2 NUMERICAL METHODS</b>   | <b>12</b> |
| 2.1 Method of characteristics . . . . .  | 12        |
| 2.2 Boundary conditions . . . . .  | 16        |
| 2.2.1 Reservoir . . . . .  | 16        |
| 2.2.2 Conduits junction . . . . .  | 16        |
| <b>3 SIMULATIONS</b>   | <b>18</b> |
| 3.1 Description of the system . . . . .  | 18        |
| 3.2 Simulation of the phenomenon . . . . .   | 19        |
| 3.3 Metrics . . . . .  | 22        |
| 3.3.1 Initial overload on the closing valve . . . . .  | 23        |
| 3.3.2 Spatial mean of the maximum overloads reached on the nodes. . . . .  | 26        |
| 3.3.3 Spatiotemporal maximum overload reached in the entire network . . . . .                                    | 28        |
| 3.3.4 Distance between the closing valve node and the node in which the<br>maximum overload is reached . . . . . | 30        |

|          |   |           |
|----------|---|-----------|
| <b>4</b> | <b>ATTEMPT TO A PREDICTIVE MODEL BASED ON NETWORK APPROACH</b>    | <b>32</b> |
| 4.1      | Simplification of the equations . . . . .                         | 32        |
| 4.1.1    | Wave branching at a junction . . . . .                            | 32        |
| 4.1.2    | Wave reflection at a reservoir . . . . .                          | 33        |
| 4.2      | Overloads computation according to the predictive model . . . . . | 34        |
| 4.3      | Wave factors correction to include dissipation effects . . . . .  | 38        |
| 4.4      | Average delay and max-first connections . . . . .                 | 40        |
| <b>5</b> | <b>PREDICTION RESULTS</b>   | <b>42</b> |
| 5.1      | Closing valve on node 16 (4,4) . . . . .                          | 43        |
| 5.2      | Closing valve on node 15 (4,3) (or specularly 12 (3,4)) . . . . . | 44        |
| 5.3      | Closing valve on node 14 (4,2) (or specularly 8 (2,4)) . . . . .  | 45        |
| 5.4      | Closing valve on node 13 (4,1) (or specularly 4 (1,4)) . . . . .  | 46        |
| 5.5      | Closing valve on node 11 (3,3) . . . . .                          | 47        |
| 5.6      | Closing valve on node 10 (3,2) (or specularly 7 (2,3)) . . . . .  | 48        |
| 5.7      | Closing valve on node 9 (3,1) (or specularly 3 (1,3)) . . . . .   | 49        |
| 5.8      | Closing valve on node 6 (2,2) . . . . .                           | 50        |
| 5.9      | Closing valve on node 5 (2,1) (or specularly 2 (1,3)) . . . . .   | 51        |
| 5.10     | Global results . . . . .  | 52        |
|          | <b>CONCLUSIONS</b>  | <b>56</b> |

# INTRODUCTION

This work of thesis is a preliminary study on the propagation of pressure waves in a square lattice hydraulic network, with a reservoir on one vertex and a valve on each of the other nodes, that can be closed to study the consequent water hammer effect.

In Chapter 1 a brief history of the scientific literature is presented, together with a summary description of the main mechanisms underlying pressure wave generation in a conduit and, then, a thorough derivation of the dynamical equations governing the phenomenon.

In Chapter 2 the method of characteristics is presented, a numerical method used to solve hyperbolic systems of coupled partial differential equations which the code used for our simulations is based on. These first two chapter take inspiration from the book by Chaundry<sup>[1]</sup>

In Chapter 3 the system studied in this work of thesis with its properties and the conditions under which the simulations are carried out are presented. The data obtained from simulation are reorganized into useful metrics to characterize the dangerousness of closing the valve on each node.

In Chapter 4 the toy model for pressure wave propagation is developed and all its limits and capabilities are shown through different analyses. .

In Chapter 5 the predictive power of the toy model described in the previous chapter is tested.

# 1. WATERHAMMER

*Waterhammer* is a term used to denote pressure fluctuations caused by a change in the flow of a fluid (water, in this case), that derives from the noise and damage they can cause on the hydraulic structures, such as pipelines, pumps and valves. Nowadays, the more general and explanatory term *hydraulic transient* is preferred. In this chapter, after a brief history of waterhammer studies, the physical phenomenon is at first described in a qualitative way to understand the main underlying mechanisms, then a thorough derivation of the equations is presented.

## 1.1 Brief history

The study of hydraulic transients began with the investigation of the propagation of sound waves in air and the propagation of waves in shallow waters, starting with Newton<sup>[2]</sup> and continuing with Euler<sup>[3],[4]</sup>, Lagrange<sup>[5]</sup> and Laplace<sup>[6]</sup>.

The first to investigate the propagation of pressure waves in pipes was Young<sup>[7]</sup>. Helmholtz, instead, pointed out that the velocity of pressure waves in water contained in a pipe was less than that in unconfined water, correctly attributing this difference to the elasticity of pipe walls.

Marey<sup>[8]</sup> conducted tests to determine the velocity of pressure waves in water and in mercury and concluded that the wave velocity was:

- independent of the amplitude of the pressure waves;
- three times greater in mercury than in water;
- proportional to the elasticity of the tube.

Korteweg<sup>[9]</sup> was the first to determine the wave velocity considering the elasticity of both the pipe wall and the fluid (earlier investigators had considered only one of the two at a time).

It is still debated who was the first, between Michaud<sup>[10]</sup> and Menabrea<sup>[11]</sup>, to deal with the problem of waterhammer, the phenomenon of interest in this work of thesis.

Gromeka<sup>[12]</sup> included the friction losses in the analysis of waterhammer for the first time. He assumed, however, that the liquid was incompressible and that the friction losses were directly proportional to the flow velocity.

Frizell<sup>[13]</sup> developed expressions for the velocity of waterhammer waves and for the pressure rise due to instantaneous reduction of the flow. Unfortunately, Frizell's work has not been appreciated as much as that of his contemporaries, Joukowski and Allievi.

In 1897, Joukowski<sup>[14]</sup> conducted extensive experiments on pipes with larger dimensions than the ones used by Weston<sup>[15]</sup> and Carpenter<sup>[16]</sup>, American engineers that failed to find agreement between theoretical and experimental results due to their pipelines being too short. He developed the relationship between the velocity reduction and the resulting pressure rise by using two methods: the conservation of energy and the continuity condition.

Allievi<sup>[17]</sup> developed the general theory of waterhammer from first principles and published it in 1902. The dynamic equation that he derived was more accurate than that of Korteweg.

Joukowski and Allievi' works have been the base for waterhammer studies of the 20th century.

Gray<sup>[2]</sup> and, later on, Lai<sup>[18]</sup> and Streeter<sup>[19]</sup> were the first to introduce and make popular the method of characteristics, invented by Monge<sup>[20]</sup> at the end of the 18th century to solve partial differential equations, for numerical waterhammer analysis.

## 1.2 Description of the phenomenon

In this section the main physical causes and properties of the waterhammer effect are described in one of the simplest examples of hydraulic system in which such phenomenon occurs.

### 1.2.1 Velocity and pressure waves

Consider the hydraulic system represented in Figure 1.1, in which a rigid pipeline is attached to a reservoir at fixed head and has a valve at distance  $L$  from the reservoir. Suppose that a compressible fluid of density  $\rho_0$  flows inside the conduit in a steady state with velocity  $V_0$  and suppose that the pressure of the reservoir is  $p_0$ .

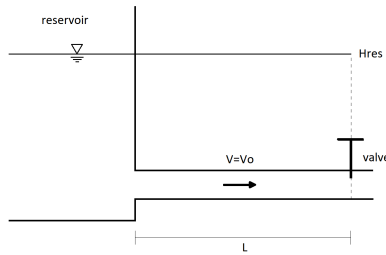


Figure 1.1: Representation of the hydraulic system in analysis in its initial conditions of homogeneous velocity  $V_0$  and pressure  $p_0$  imposed by the reservoir head level  $H_{res}$ .

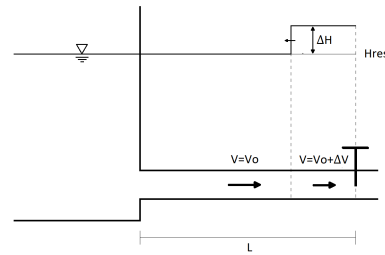


Figure 1.2: Representation of the hydraulic system in analysis after the modification of the valve opening area, causing the propagation of pressure and velocity waves.

As displayed in Figure 1.2, if the valve opening is instantaneously changed at time  $t = 0$ , in the proximity of the valve the fluid velocity, pressure and density become  $V_0 + \Delta V$ ,  $p_0 + \Delta p$  and  $\rho_0 + \Delta \rho$ , respectively. Such variations propagate upstream with velocity  $a$ . From the point of view of an observer moving together with the wave front, that in this inertial reference frame is stationary, the fluid upstream moves with velocity  $V_0 + a$ , whereas downstream it moves with velocity  $V_0 + \Delta V + a$ . Neglecting friction, the force acting on the fluid in a small control volume, computed as the momentum rate of change, is

$$F = \rho_0(V_0 + a)A\Delta V \approx \rho_0 a A \Delta V,$$

where  $A$  is the section of the conduit and the approximation can be done since  $a \gg V_0$  as confirmed by numerous experimental data.

Since the net force is given by  $F = -A\Delta p$  and recalling the piezometric head expression  $H = \rho g p$ , one obtains

$$\Delta H = \pm \frac{a}{g} \Delta V, \quad (1.1)$$

where the minus sign indicates an increase (or decrease) of the pressure in correspondence of a decrease (or increase) in velocity. This happens if the velocity variation occurs downstream; if it happens upstream a plus sign shall be put in Equation (1.1), so that to a pressure increase (or decrease) would correspond to a velocity increase (or decrease).

In the control volume, the mass variation due to the density change is negligible. Then, the continuity equation imposes the mass inflow  $\rho_0 A(V_0 + a)$  and the mass outflow  $(\rho_0 + \Delta\rho)A(V_0 + \Delta V + a)$  to be equal, so that

$$\Delta V = -\frac{\Delta\rho}{\rho_0}(V_0 + \Delta V + a) \approx -\frac{\Delta\rho}{\rho_0}a, \quad (1.2)$$

where the approximation is again due to  $a \gg V_0 + \Delta V$ . Recalling the definition of the bulk modulus of elasticity of a fluid  $K = \rho_0 \frac{\Delta p}{\Delta\rho}$ , putting together Equations (1.1) and (1.2) and making explicit the wave speed one obtains

$$a = -K \frac{\Delta V}{\Delta p} = \frac{K}{a\rho_0}. \quad (1.3)$$

Finally, one obtains a formula for the velocity of propagation of the pressure waves in a rigid pipeline:

$$a = \sqrt{\frac{K}{\rho_0}}. \quad (1.4)$$

For a thorough derivation of the pressure and velocity waves' speed in the case of elastic pipe walls, see Section 1.3

## 1.2.2 The four phases

Consider the same system as before, in which the fluid has initial velocity  $V_0 > 0$  (it flows downstream) and initial head  $H_{res}$  imposed by the reservoir (Figure 1.3a). Suppose we close the valve instantaneously at time  $t = 0$ . At the valve, the velocity changes from  $V = V_0$  to  $V = 0$ , since the closure of the valve imposes null velocity in its proximity, so  $\Delta V = -V_0$ .

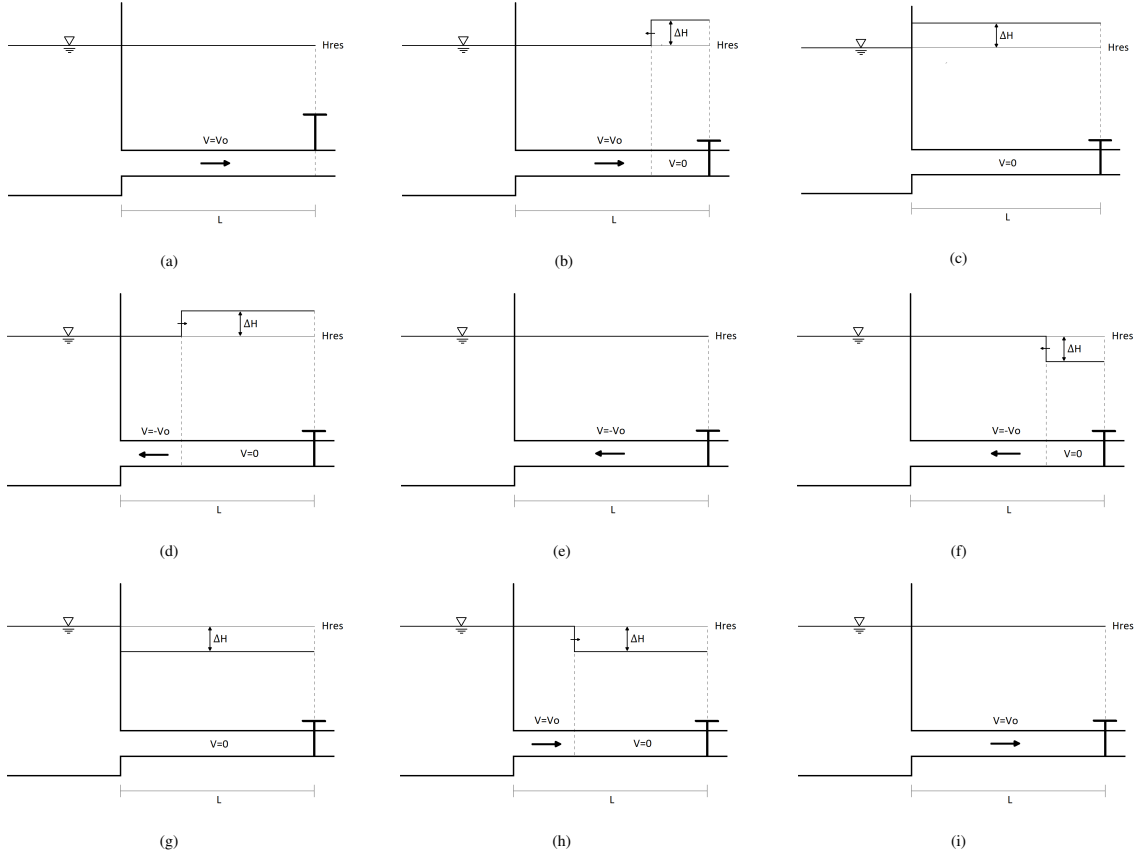


Figure 1.3: Representation of the development of the four phases of the waterhammer phenomenon.

From Equation (1.1) we know that the head variation is now  $\Delta H = \frac{a}{g}V_0$ , so there's an increase in pressure (Figure 1.3b). The pressure and velocity waves propagate with speed  $a$  towards the reservoir. At time  $t = \frac{L}{a}$ , the pressure in the entire pipeline is  $H_{res} + \frac{a}{g}V_0$  and the fluid is still (Figure 1.3c). Once the reservoir is reached, it imposes its head value  $H_{res}$ , so that another abrupt pressure variation  $\Delta H = -\frac{a}{g}V_0$  occurs upstream. This causes a velocity variation  $\Delta V = -V_0$  (Figure 1.3d). At time  $t = 2\frac{L}{a}$ , the pressure in the entire pipeline is  $H_{res}$  and the velocity  $V = -V_0$  (Figure 1.3e). Once the valve is reached again, null velocity is imposed but the velocity variation is now positive,  $\Delta V = V_0$ , so the head variation is negative,  $\Delta H = -\frac{a}{g}V_0$  (Figure 1.3f). At time  $t = 3\frac{L}{a}$  the wave has propagated back to the reservoir and in the pipeline the fluid is still and at a head level  $H = H_0 - \frac{a}{g}V_0$  (Figure 1.3g). Again, at the reservoir the head value  $H_{res}$  is imposed, so that  $\Delta H = \frac{a}{g}V_0$  and  $\Delta V = V_0$  (Figure 1.3h). At time  $t = 4\frac{L}{a}$ , the initial conditions are restored in the entire pipeline:  $H = H_{res}$  and  $V = V_0$  (Figure 1.3i). Then, the cycle starts over.

In summary, the waterhammer phenomenon develops in four periodic phases:

- 1<sup>st</sup> phase: initial condition with the fluid at reservoir head level flowing rightwards;
- 2<sup>nd</sup> phase: the fluid is still and the head is above the reservoir level;
- 3<sup>rd</sup> phase: the fluid is at the reservoir head level but flows leftwards;
- 4<sup>th</sup> phase: the fluid is still again, but the head level is below the reservoir's.

The time interval over which the phenomenon develops in its four phases is

$$T = 4\frac{L}{a}, \quad (1.5)$$

that is the time necessary for the wave to propagate through the conduit two times, back and forth.

Ideally, the alternation of the four phases goes on forever, but in real systems the wave amplitude is damped by dissipation and the phenomenon, still maintaining its periodic behaviour, loses intensity over time.

## 1.3 Equations of motion

In this section I present a derivation of the dynamic and continuity equations characterizing an unsteady flow through closed conduits. The assumptions under which these calculations are carried out are the following:

- flow is one dimensional and the velocity distribution is uniform over the cross section of the conduit;
- the conduit walls and the fluid are linearly elastic;
- formulas for computing the steady-state friction losses are valid during the transient state.

### 1.3.1 Dynamic equation

Consider a horizontal element of fluid with cross-sectional area  $A$  and length  $\delta x$ , within a conduit (Figure 1.4). If at position  $x$  the head and discharge values are  $H$  and  $Q$ , at position  $x + \delta x$  they are  $H + \frac{\partial H}{\partial x} \delta x$  and  $Q + \frac{\partial Q}{\partial x} \delta x$ , respectively.

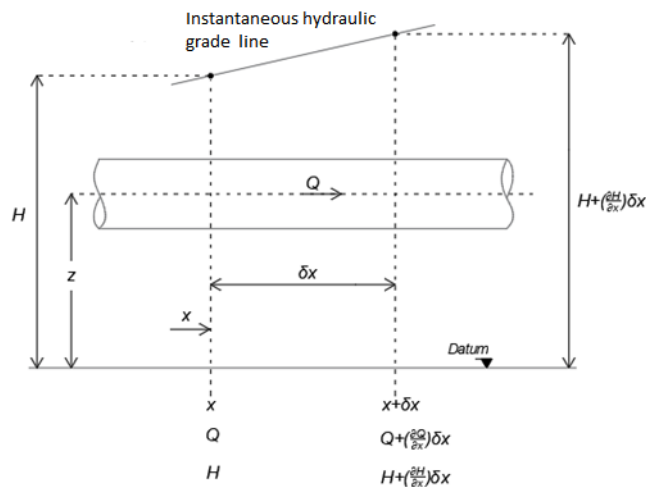


Figure 1.4: Representation of the infinitesimal control volume used to develop the dynamic equation.

In the horizontal direction three main forces are acting on the fluid element, as shown in Figure 1.5: pressure forces,

$$F_1 = \gamma A(H - z) \quad (1.6)$$

and

$$F_2 = \gamma A\left(H + \frac{\partial H}{\partial x} \delta x - z\right), \quad (1.7)$$

and the shear force due to friction given by the Darcy-Weisbach formula,

$$S = \frac{\gamma f V^2}{g} \pi D \delta x, \quad (1.8)$$

where  $\gamma$  is the specific weight,  $z$  is the vertical coordinate,  $g$  is the gravitational acceleration,  $f$  is the friction factor and  $D$  is the conduit diameter.

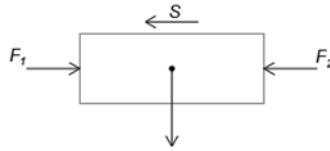


Figure 1.5: Scheme of the forces acting on the control volume.

The resultant horizontal force is

$$F = \gamma A \frac{\partial H}{\partial x} \delta x - \frac{\gamma f V^2}{g} \pi D \delta x, \quad (1.9)$$

so that Newton's second law of motion, divided by the mass of the fluid element  $\frac{\gamma}{g} A \delta x$ , gives

$$\frac{dV}{dt} = -g \frac{\partial H}{\partial x} - \frac{f V^2}{2D}. \quad (1.10)$$

Writing the material derivative as  $\frac{dV}{dt} = \frac{\partial V}{\partial t} + V \frac{\partial V}{\partial x} \approx \frac{\partial V}{\partial t}$ , that's shown to be a good approximation by Allievi, and replacing  $V^2$  with  $V|V|$ , in order to account for the shear force acting on the opposite direction with respect to the fluid's flow, one obtains the following dynamic equation, expressed in terms of the discharge  $Q$ :

$$\frac{\partial Q}{\partial t} + gA \frac{\partial H}{\partial x} + \frac{f}{2DA} Q|Q| = 0, \quad (1.11)$$

### 1.3.2 Continuity equation

Consider a fluid element as in Figure 1.6. The volume inflow and outflow are, respectively,

$$\mathcal{V}_{in} = V \pi r^2 \delta t, \quad (1.12)$$

$$\mathcal{V}_{out} = \left( V + \frac{\partial V}{\partial x} \delta x \right) \pi r^2 \delta t, \quad (1.13)$$

so that the net volume inflow is

$$\delta \mathcal{V}_{in} = \mathcal{V}_{in} - \mathcal{V}_{out} = \frac{\partial V}{\partial x} \delta x \pi r^2 \delta t. \quad (1.14)$$

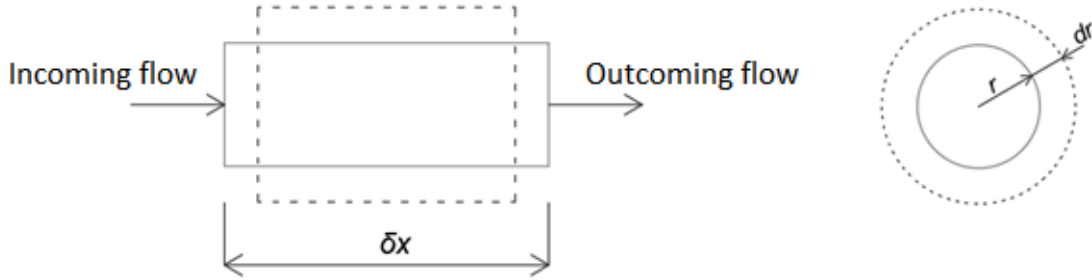


Figure 1.6: Scheme of the volume changes due to net incoming flow and section area modification.

The volume change due to the fluid compressibility is

$$\delta \mathcal{V}_c = -\frac{\delta p}{K} \mathcal{V} = -\frac{\partial p}{\partial t} \frac{\delta t}{K} \pi r^2 \delta x, \quad (1.15)$$

where  $K$  is the bulk modulus of elasticity of the fluid and the pressure change has been written as  $\delta p = \frac{\partial p}{\partial t} \delta t$ .

The Young's modulus of elasticity under the linearly elastic conduit walls assumption is

$$E = \frac{\delta \sigma}{\delta \varepsilon} = \frac{\partial p}{\partial t} \delta t \frac{r^2}{e \delta r}, \quad (1.16)$$

where  $e$  is the conduit walls' thickness,  $\delta \sigma = \delta p \frac{r}{e}$  is the change in hoop stress and  $\delta \varepsilon = \frac{\delta r}{r}$  is the change in strain.

The radius change is, then,

$$\delta r = \frac{\partial p}{\partial t} \frac{r^2}{e E} \delta t. \quad (1.17)$$

The total volume change, written in terms of the conduit radius change, is

$$\delta\mathcal{V}_r = 2\pi r \delta r \delta x = 2\pi \frac{\partial p}{\partial t} \frac{r^3}{eE} \delta t \delta x, \quad (1.18)$$

but it is also given by the sum of the net volume inflow and the volume change due to the fluid compressibility, both previously computed:

$$\delta\mathcal{V}_r = \delta\mathcal{V}_{in} + \delta\mathcal{V}_c. \quad (1.19)$$

Substituting Equations (1.12), (1.15) and (1.18) into Equation (1.19), one obtains

$$\frac{\partial V}{\partial x} + \frac{\partial p}{\partial t} \left( \frac{2r}{eE} + \frac{1}{K} \right) = 0, \quad (1.20)$$

which can be written in terms of the fluid discharge and head as

$$\frac{a^2}{gA} \frac{\partial Q}{\partial x} + \frac{\partial H}{\partial t} = 0, \quad (1.21)$$

where

$$a = \sqrt{\frac{K}{\rho \left( 1 + \frac{KD}{eE} \right)}} \quad (1.22)$$

is the discharge and head waves' velocity in case of elastic conduit walls.

In summary, the dynamic equation (1.11) and the continuity equation (1.21) constitute a system of coupled hyperbolic partial differential equations, that cannot be solved analitically, so one has to resort to numerical methods. In Chapter 2, the method of characteristics is presented, since it is the numerical method used for the numerical simulations carried out in this work of thesis.

## 2. NUMERICAL METHODS

In this chapter the method of characteristics is presented. It is a numerical method that allows to reduce a hyperbolic system of coupled differential equations to linear differential equations, thanks to an appropriate discretization of space and time specific for waves propagation in hydraulic transients. Its convergence and stability are briefly discussed and, at the end of the chapter, boundary conditions for the system studied in this work of thesis are listed.

### 2.1 Method of characteristics

Calling the derived dynamical equations

$$L_1 = \frac{\partial Q}{\partial t} + gA \frac{\partial H}{\partial x} + \frac{f}{2DA} Q|Q| = 0, \quad (2.1)$$

$$L_2 = \frac{\partial Q}{\partial x} + \frac{gA}{a^2} \frac{\partial H}{\partial t} = 0, \quad (2.2)$$

any linear combination would also be null,  $L_1 + \lambda L_2 = 0$ , for any  $\lambda$ . Expanding such equation, one obtains

$$\left( \frac{\partial Q}{\partial t} + \lambda \frac{\partial Q}{\partial x} \right) + \frac{\lambda gA}{a^2} \left( \frac{\partial H}{\partial t} + \frac{a^2}{\lambda} \frac{\partial H}{\partial x} \right) + \frac{f}{2DA} Q|Q| = 0. \quad (2.3)$$

If  $Q(x, t)$  and  $H(x, t)$  are solutions of such equation, their total derivative can be written as

$$\frac{dQ}{dt} = \frac{\partial Q}{\partial t} + \frac{dx}{dt} \frac{\partial Q}{\partial x} \quad \text{and} \quad \frac{dH}{dt} = \frac{\partial H}{\partial t} + \frac{dx}{dt} \frac{\partial H}{\partial x}, \quad (2.4)$$

respectively. So, by defining  $\frac{dx}{dt} = \lambda = \frac{a^2}{\lambda}$ , that gives  $\lambda = \pm a$ , Equation (2.3) can be finally written as

$$\frac{dQ}{dt} \pm \frac{gA}{a} \frac{dH}{dt} + \frac{f}{2DA} Q|Q| = 0, \quad \text{if} \quad \frac{dx}{dt} = \pm a. \quad (2.5)$$

In this way two different ordinary differential equations in the independent variable  $t$  were derived from a hyperbolic system of two coupled partial differential equations, at the price of restricting their validity to the so called *characteristic lines* of slope  $\pm \frac{1}{a}$  in the  $x$ - $t$  plane.

Consider the simple system described in the previous chapter, represented in Figure 1.1, and imagine to instantaneously close the valve at time  $t = 0$ . Then, pressure and velocity waves start propagating in the upstream direction at speed  $a$ , so in the  $x-t$  plane the characteristic line with slope  $-\frac{1}{a}$  passing by the point  $(L, 0)$  represents the travelling path of such perturbations, dividing the plane in the lower region (I), dominated by initial conditions, and the upper region (II) influenced by the boundary condition that impose the transient state (Figure 2.1).

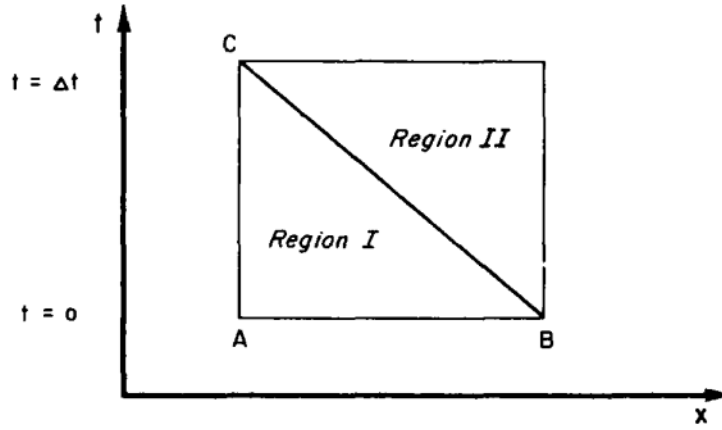


Figure 2.1: Characteristic line in the case of perturbation at the downstream end of a conduit. It divides the  $x-t$  plane in a region dominated by the initial conditions (Region I) and a region dominated by the boundary conditions imposing the transient state (Region II).

Exploiting a first order finite-difference technique, in which space and time are discretized so that  $\Delta x = a\Delta t$ , it is possible to compute head and discharge in a point  $P = (x_P, t_P)$  in the  $x-t$  plane, knowing their value in points  $A = (x_P - \Delta x, t_P - \Delta t)$  upstream and  $B = (x_P + \Delta x, t_P - \Delta t)$  downstream (Figure 2.2).

In fact, writing

$$\Delta Q = Q_P - Q_A, \quad \Delta H = H_P - H_A \quad (2.6)$$

along the  $C^+$  line and

$$\Delta Q = Q_P - Q_B, \quad \Delta H = H_P - H_B \quad (2.7)$$

along the  $C^-$  line, Equations 2.5 become

$$Q_P - Q_A + \frac{gA}{a}(H_P - H_A) + \frac{f\Delta t}{2DA}Q_A|Q_A| = 0 \quad \text{along } C^+ \quad (2.8)$$

and

$$Q_P - Q_B - \frac{gA}{a}(H_P - H_B) + \frac{f\Delta t}{2DA}Q_B|Q_B| = 0 \quad \text{along } C^-. \quad (2.9)$$

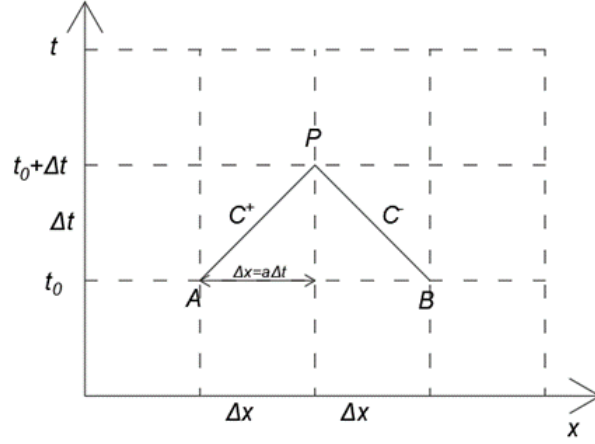


Figure 2.2: Representation of the characteristics lines  $C^+$  and  $C^-$  used to derive the flow and head in point P, starting from precomputed A and B points, in the discretized  $t$ - $x$  plane.

Defining  $C_a = \frac{gA}{a}$  and

$$C_p = Q_A + C_a H_A - \frac{f \Delta t}{2DA} Q_A |Q_A|, \quad (2.10)$$

$$C_n = Q_B - C_a H_B - \frac{f \Delta t}{2DA} Q_B |Q_B|, \quad (2.11)$$

one obtains the positive and negative characteristic equations

$$Q_P = C_p - C_a H_P, \quad (2.12)$$

$$Q_P = C_n + C_a H_P. \quad (2.13)$$

Solving for the unknowns  $Q_P$  and  $H_P$ , one obtains:

$$Q_P = \frac{C_p + C_n}{2}, \quad (2.14)$$

$$H_P = \frac{C_p - C_n}{2C_a}. \quad (2.15)$$

As shown in Figure 2.3, these equations can be used to compute the discharge and head evolution in the internal points of the pipelines (white circles), but for the extremal points a combination of such equations with some boundary conditions is needed. For example in the downstream end of a conduit (triangles) one should use Equation (2.12) plus an appropriate boundary condition, whereas in the upstream end (black circles) one should use Equation (2.13) plus an appropriate boundary condition.

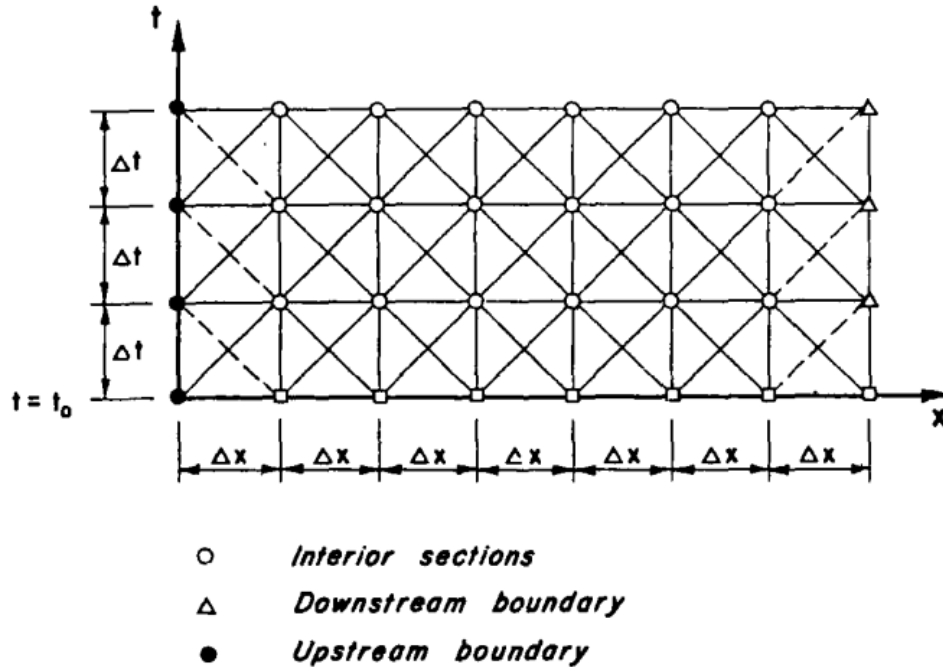


Figure 2.3: Discharge and head values in points at time  $t$  are used to compute discharge and head values in points at time  $t + \Delta t$ . The characteristic equations are combined with boundary conditions when needed at the extremal points.

It's been shown that for this numerical method convergence means stability and vice versa. It has also been found that the stability condition is

$$\frac{\Delta t}{\Delta x} \leq \frac{1}{a} \tag{2.16}$$

and is called the *Courant's stability condition*.

In the next section are derived useful boundary conditions for the system studied in this work of thesis.

## 2.2 Boundary conditions

In the following subsections boundary conditions are derived in the case of the presence of a reservoir at fixed head level and in the case of various conduits converging in and diverging from a junction. In both derivations, it is assumed that the velocity head and head losses are negligible.

### 2.2.1 Reservoir

Consider a conduit connected to a reservoir. The head in the conduit end attached to the reservoir is fixed:

$$H_P = H_{res}. \quad (2.17)$$

The characteristic equation to use depends on the relative position of the reservoir: if it's upstream, the negative characteristic Equation (2.13) gives

$$Q_P = C_n + C_a H_{res}, \quad (2.18)$$

whereas, if it is downstream, the positive characteristic Equation (2.12) gives

$$Q_P = C_p - C_a H_{res}. \quad (2.19)$$

### 2.2.2 Conduits junction

Consider a junction of  $n$  convergent conduits (labeled with numbers from 1 to  $n$ ) and  $m$  divergent conduits (labeled with number from  $n + 1$  to  $n + m$ ). Suppose the conduits are all of the same length, so that they're all divided into the same number  $l$  of sections when discretizing space. The head at the last section of converging conduits (section labeled by  $l + 1$ ) and at the beginning of diverging conduits (section labeled by 1) of the conduits is set to be equal:

$$H_P \equiv H_{P_{i,l+1}} = H_{P_{j,1}} \quad \text{for } i \in \{1, \dots, n\}, j \in \{n + 1, \dots, n + m\}. \quad (2.20)$$

The continuity equation requires the following condition:

$$\sum_{i=1}^n Q_{P_{i,l+1}} = \sum_{j=n+1}^{n+m} Q_{P_{j,1}} + Q_v, \quad (2.21)$$

where the term

$$Q_v = A_v c_v \sqrt{2gH_P} \quad (2.22)$$

stands for an eventual leakage due to a valve positioned on the junction node.  $A_v$  is the valve opening area,  $c_v = 0.61$  is the *vena contracta* coefficient and  $g$  the gravitational acceleration. The discharge values are computed with the positive or negative characteristic equation depending on the conduit converging in or diverging from the junction, respectively:

$$Q_{P_{i,l+1}} = C_{p_i} - C_{a_i} H_P \quad \text{for } i \in \{1, \dots, n\}, \quad (2.23)$$

$$Q_{P_{j,1}} = C_{n_j} + C_{a_j} H_P \quad \text{for } j \in \{n+1, \dots, n+m\}. \quad (2.24)$$

Combining Equations (2.21), (2.23) and (2.24), one obtains

$$\sum_{i=1}^n C_{p_i} - \sum_{i=n+1}^{n+m} C_{n_i} - \sum_{i=1}^{n+m} C_{a_i} H_P = A_v c_v \sqrt{2gH_P}. \quad (2.25)$$

Then, defining

$$k_1 = \sum_{i=1}^{n+m} C_{a_i}, \quad (2.26)$$

$$k_2 = \sum_{i=1}^n C_{p_i} - \sum_{i=n+1}^{n+m} C_{n_i} \quad (2.27)$$

and squaring Equation (2.25), one obtains:

$$k_1^2 H_P^2 - 2k_3 H_P + k_2^2 = 0, \quad (2.28)$$

where  $k_3 = k_1 k_2 + (A_v c_v)^2 g$ . Finally,

$$H_P = \frac{k_3 + \sqrt{k_3^2 - k_1^2 k_2^2}}{k_1^2}. \quad (2.29)$$

In the case of closed valve the previous formula reduces to a simpler form:

$$H_P = \frac{k_2}{k_1} = \frac{\sum_{i=1}^n C_{p_i} - \sum_{i=n+1}^{n+m} C_{n_i}}{\sum_{i=1}^{n+m} C_{a_i}}. \quad (2.30)$$

In order to obtain the discharges in the different conduits one can substitute  $H_P$  with the derived formula inside Equations (2.23) and (2.24).

### 3. SIMULATIONS

In this chapter, it is described how we carried out the simulations of the phenomenon from which we obtained the data to elaborate and analyze, with the purpose of finding common patterns and trends amongst different-located nodes and different-sized networks.

#### 3.1 Description of the system

The system studied in this work of thesis is a hydraulics network. Its geometrical structure is that of a square lattice with  $n$  conduits per side. A water reservoir at fixed head is positioned on the bottom-left vertex of the square. On each node there is a valve with area  $A_v$ , which is adjustable and supplies water to a user. In Fig. 3.1 such network is represented for  $n = 3$ . The elastic pipelines, which have circular section, have length  $L$ , diameter  $D$ , wall thickness  $e$ , roughness  $\varepsilon$  and Young modulus  $E$ .

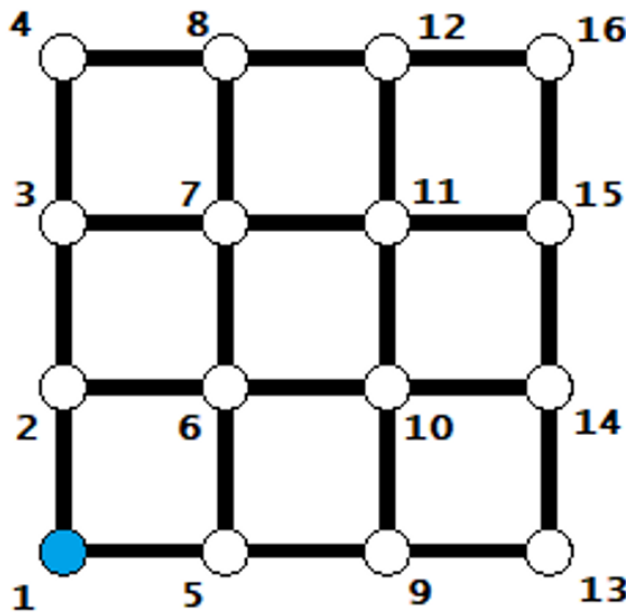


Figure 3.1: Square lattice network with  $n = 3$  conduits per side, with a total of  $(n + 1)^2 = 16$  nodes. The nodes are numbered from below upwards, from left to right.

## 3.2 Simulation of the phenomenon

The initial condition of the system is that of a fluid in permanent motion inside the network and it is computed taking into account the head losses due to both the leakage on each open valve and, to a lesser extent, the conduit walls' roughness. We've used a simulation code already written for previous works of thesis, that we integrated with an EPANET software for an accurate computation of the initial conditions.

A simulation consists in closing at the time instant  $t_b$  one of the valves in a period of time  $\Delta t_c$  and let the fluid's head and flow evolve in the network, according to the equations obtained with the method of characteristics and the appropriate boundary conditions. Recalling that, in the simple example of Chapter 1, Section 1.2.2, the period of time in which the phenomenon develops in its four phases is given by Equation (1.5), we let the system evolve during a period of time  $t_s = 2\frac{4d}{a}$ , where  $d = 2nL$  is the diameter of the network, so as to observe at least a couple of complete head oscillations on the different nodes.

|                          |               |   |
|--------------------------|---------------|---|
| Reservoir head           | $H_{res}$     | 50m   |
| Water density            | $\rho_a$      | 1000 $\frac{\text{kg}}{\text{m}^3}$           |
| Bulk modulus             | $K_a$         | $2.19 \cdot 10^9 \frac{\text{N}}{\text{m}^2}$ |
| Conduit length           | $L$           | 100m  |
| Conduit diameter         | $D$           | 0.25m   |
| Conduit walls' thickness | $e$           | 0.01m   |
| Conduit walls' roughness | $\varepsilon$ | 0.001m  |
| Conduit Young modulus    | $E$           | $200 \cdot 10^9 \frac{\text{N}}{\text{m}^2}$  |
| Closing valve area       | $A_{v,c}$     | $0.001\text{m}^2$                             |
| Other valves area        | $A_{v,s}$     | $0.0001\text{m}^2$                            |

Table 3.1: List of the physical properties of the fluid (water) and of the pipelines and values assigned to them in the simulations.

In Tab 3.1 are displayed the values of the various physical quantities used in the simulations. Notice that the closing valve area is one order of magnitude greater than that of the other valves. This difference is heritage of a previous work of thesis, which had the objective of identifying the position of a bigger valve inside a network, knowing the head variations on all the nodes caused by the closing of such valve.

The pressure wave generated in this system has speed  $a = 1311 \frac{\text{m}}{\text{s}}$ . The discrete time unit is  $dt = 0.01\text{s}$ . The Courant stability condition, expressed in Equation (2.16), imposes a lower bound for the discretization of space:  $dx \geq a \cdot dt = 13,11\text{m}$ . A good choice would be

$$dx = \frac{L}{\lfloor \frac{L}{a \cdot dt} \rfloor} = \frac{\frac{L}{a \cdot dt}}{\lfloor \frac{L}{a \cdot dt} \rfloor} a \cdot dt \geq a \cdot dt$$

so as to have the larger possible amount of equidistant points in which head and flow are computed inside a conduit. In this specific case  $L=100\text{m}$ , so  $dx = 14,28\text{m}$ .

Once the pressure and velocity profiles are obtained in the entire network, it is possible to derive the time evolution of the pressure on each node, thence the time evolution of the pressure difference with respect to the initial pressure. In Figure 3.2 such profiles are reported for every node of a  $n = 3$  square network, upon closing at time  $t_b = 0.5\text{s}$  the valve on the bottom-right vertex (node 13) in a time interval  $\Delta t_c = 0.01\text{s}$ .

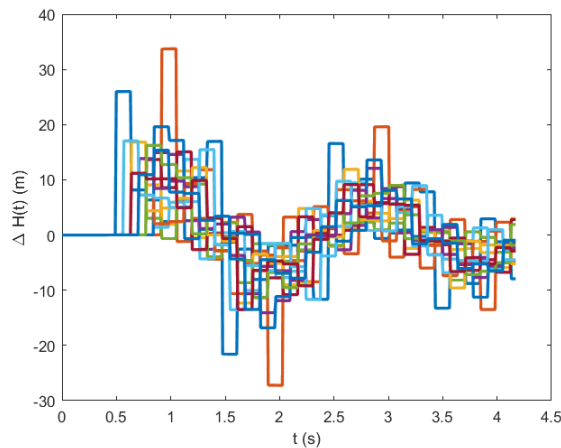


Figure 3.2: Time evolution of the overloads on all the nodes of the  $n = 3$  square lattice network.

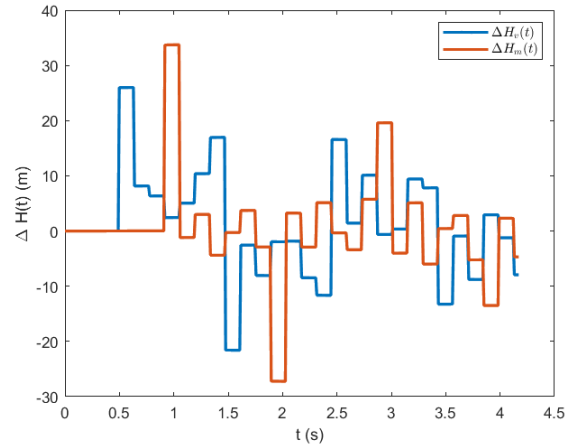


Figure 3.3: Time evolution of the overloads on the closing valve node (node 13, blue) and on the node in which the maximum overload is reached (node 4, red).

Figure 3.3 highlights the time evolution of the overload on the closing valve node and the node in which the maximum overload is reached over time. It is interesting to notice that the maximum overload is not reached on the closing valve node, but on the vertex opposite to it (node 4). This example already shows how the effects are strongly non-local.

### 3.3 Metrics

We've run simulations for networks with a number of conduits per side ranging from  $n = 3$  to  $n = 11$ . For each network we've studied the water hammer effects, positioning the closing valve on each node of the lattice. From the obtained data, we've computed metrics to condensate information into. In this way we can characterize each node with a value, which is representative of the effects of closing the valve on that same node.

The metrics found relevant are listed below:

- the initial overload reached on the closing valve node  $v$  immediately after the closure,  $\Delta H_{v,i} = \Delta H_v(t_b)$ ;
- the spacial mean of the overload maxima reached on all the nodes (excluded the first node, on which the pressure is kept constant by the reservoir),

$$\Delta H_{MEAN} = \frac{1}{n_{nodes} - 1} \sum_{j=2}^{n_{nodes}} \max_t \Delta H_j(t);$$

- the maximum overload reached in the entire network over time,

$$\Delta H_{MAX} = \max_j \max_t \Delta H_j(t);$$

- the distance between the closing valve node and the node in which the maximum overload is reached,  $d(v, m)$ , where

$$m = \arg \max_j \max_t \Delta H_j(t).$$

In the computation of the overall maximum, the initial overload on the closing valve node is excluded in order to investigate only the effects subsequent to the closure, taking into account the possibility that the maximum could be reached on the same closing valve node at a later time.

### 3.3.1 Initial overload on the closing valve

The initial overload on the closing valve is a strongly local metric, because it topologically depends only on the number of nearest neighbors of the closing valve node.

Suppose the closing valve is on a junction of  $n$  converging conduits and  $m$  diverging conduits (with the labeling used in Chapter 2 in the definition of the boundary conditions), all with the same physical properties. Before the closing of the valve

$$\sum_{i=1}^n Q_i = \sum_{j=n+1}^{n+m} Q_j + Q_v, \quad (3.1)$$

where  $Q_v$  is given by 2.22. Neglecting dissipative effects, Equations 2.10 and 2.11 become

$$C_{p_i} = Q_i + C_a H, \quad (3.2)$$

$$C_{n_j} = Q_j + C_a H, \quad (3.3)$$

where  $H$  is the head before the closing of the valve. The head after the closure  $H'$ , given by Equation 2.30, can be written as follows:

$$H' = \frac{\sum_{i=1}^n Q_i - \sum_{j=n+1}^{n+m} Q_j + (n+m)C_a H}{(n+m)C_a} = \frac{Q_v}{(n+m)C_a} + H. \quad (3.4)$$

Under this assumptions, the initial overload on the closing valve is, finally,

$$\Delta H_{v,i} = \frac{4a}{\pi D^2} c_v A_v \sqrt{\frac{2H_v(0)}{g} \frac{1}{nn_v}}, \quad (3.5)$$

where  $nn_v$  is the number of nearest neighbors of node  $v$ , the closing valve node.

In Figure 3.4 is reported the initial overload relative to the square root of the starting head level on the closing valve node as a function of the number of its nearest neighbors. The data are taken from the simulations run on different sized square lattice networks and they are in good agreement with Equation 3.5, despite neglecting the dissipative effects.

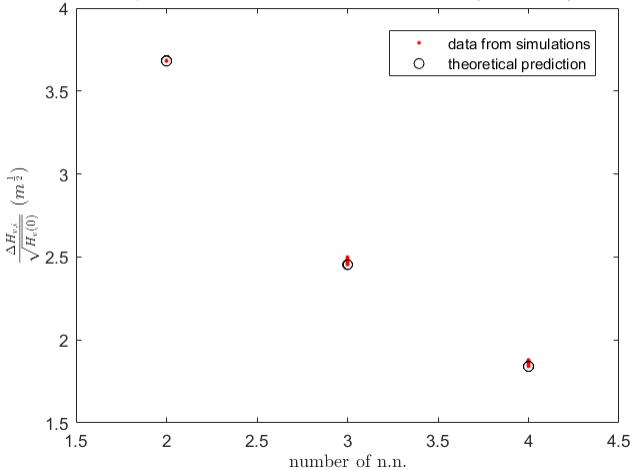


Figure 3.4: The theoretical (black circles) and simulated (red dots) initial overloads relative to the square roots of the steady state head level are plotted against the number of nearest neighbors of the closing valve node.

The dependence of the initial overload on the size of the network only passes through the initial head level, which decreases both with the increasing of the distance from the reservoir and with the enlarging of the network, as shown in Figure 3.5.

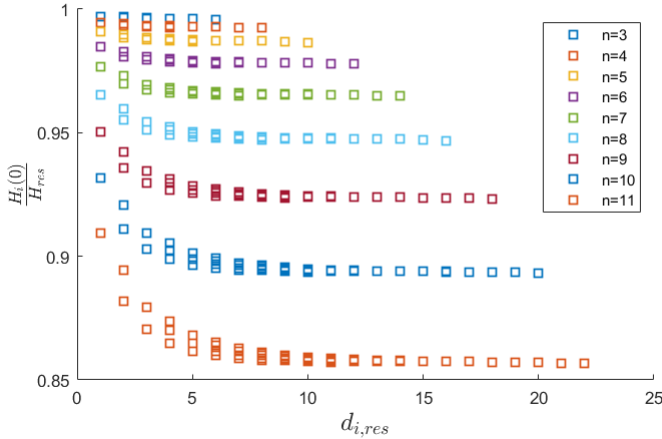


Figure 3.5: Trend of the steady state head level on the closing valve node relative to the reservoir head level as a function of the distance from the reservoir and of the size of the network.

Figure 3.6 lists the histograms for different-sized networks, representing the initial overload reached on the closing valve nodes immediately after the closure.

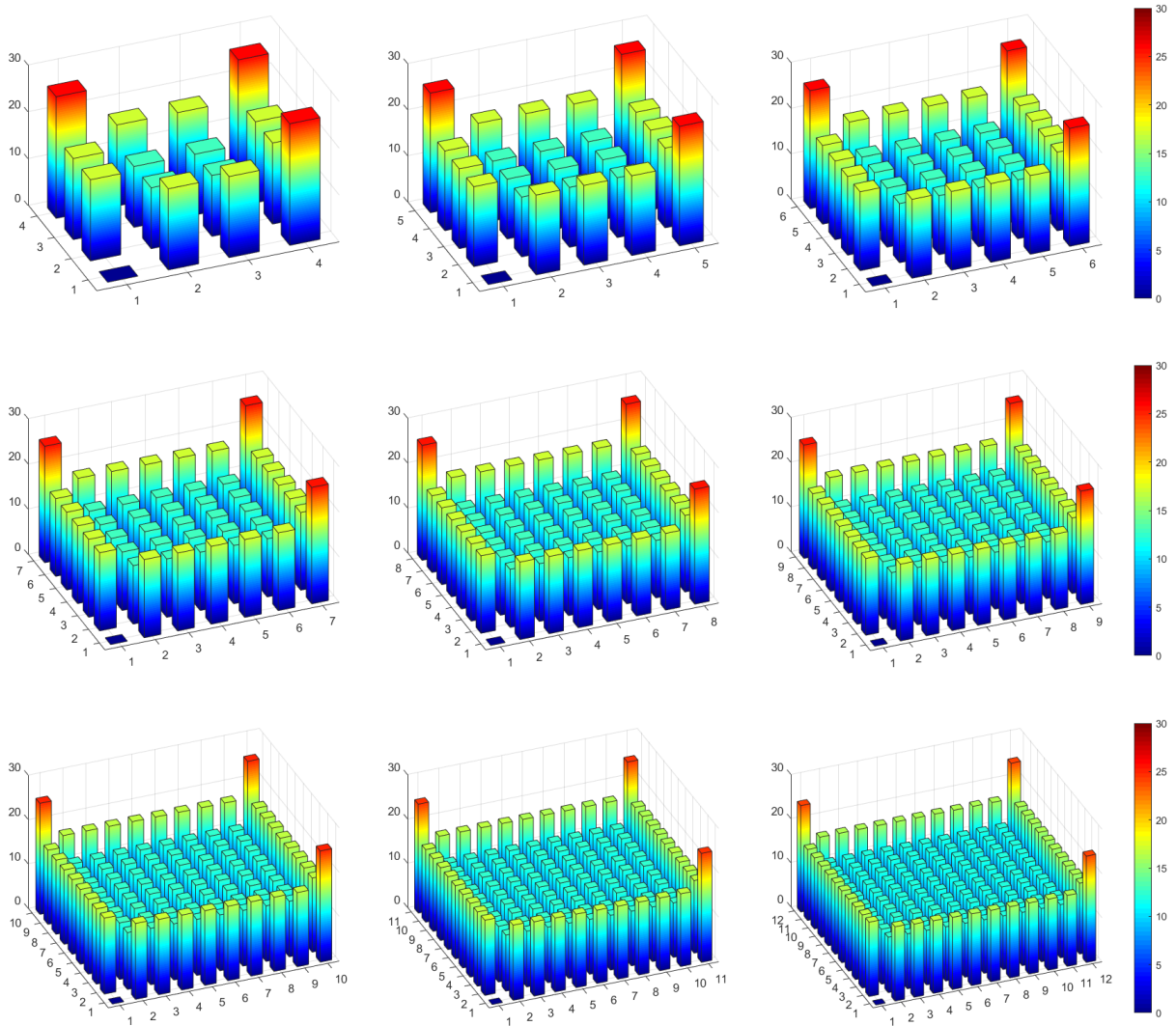


Figure 3.6: Initial overload on the closing valve metric displayed for the different nodes of the  $n = 3$  to  $n = 11$  square lattice networks. On the vertical axis, the overload is measured in  $m$ .

### 3.3.2 Spatial mean of the maximum overloads reached on the nodes.

The spacial mean of the the temporal maxima reached on every node of the network is a good metric for visualizing the effect that closing the valve on a node has on the entire network. In Figure 3.7 the histograms representing such metric show how the effects are stronger if closing valves on vertices and how they get weaker and weaker going towards the center of the network and towards the reservoir.

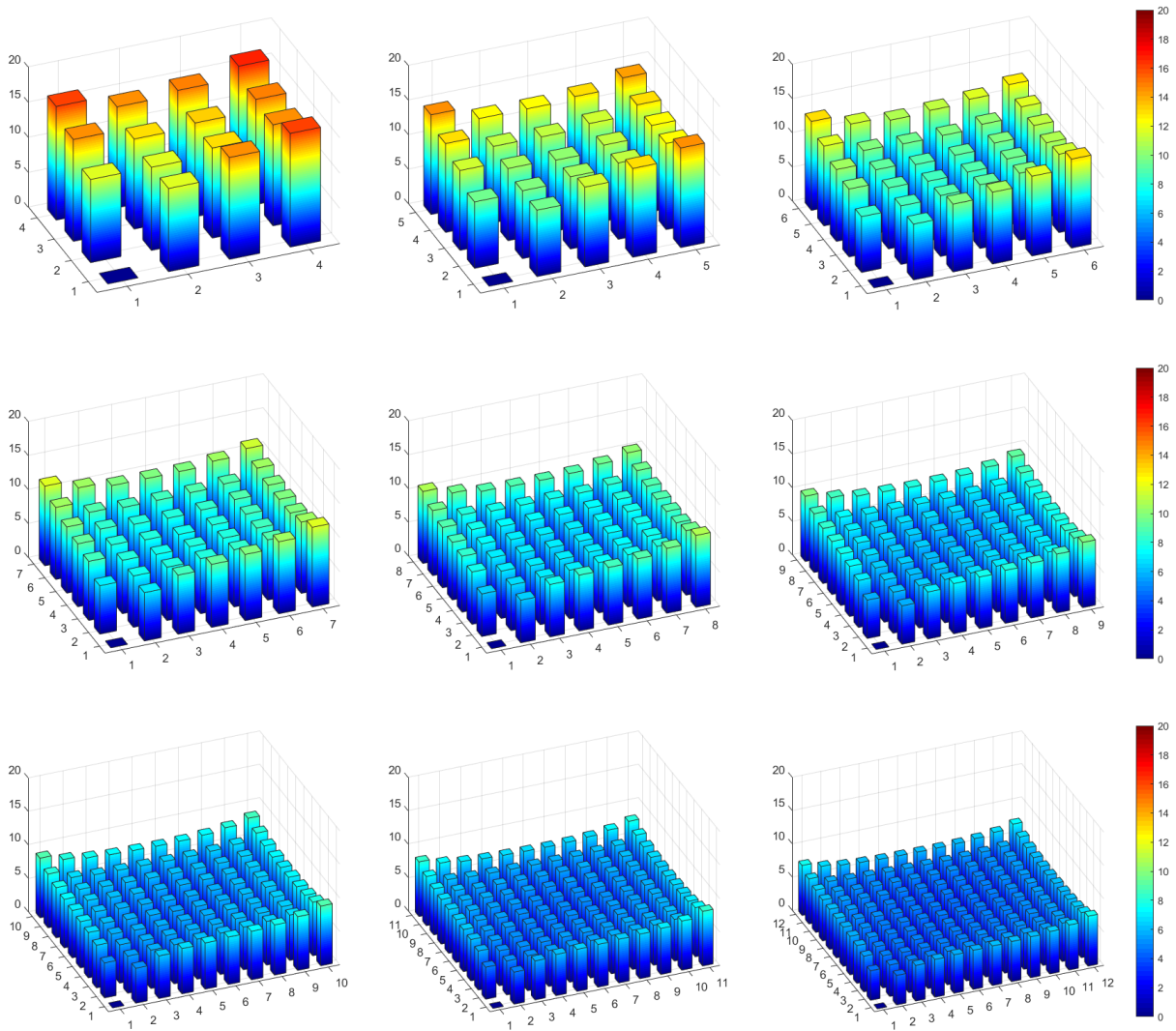


Figure 3.7: Spatial mean of maximum overloads metric displayed for the different nodes of the  $n = 3$  to  $n = 11$  square lattice networks. On the vertical axis, the overload is measured in  $m$ .

One can also normalize such metric with respect to the initial overload on the valve, in order to understand the average effect of closing the valve on a certain node, relative to the initial effect on the same closing valve node. In Figure 3.8 it can be seen how the behaviour of the previous histograms is maintained, but within nodes with the same number of nearest neighbors. In particular, vertices present the lowest average relative effect and internal nodes nearer to vertices have the highest average relative effect on the network.

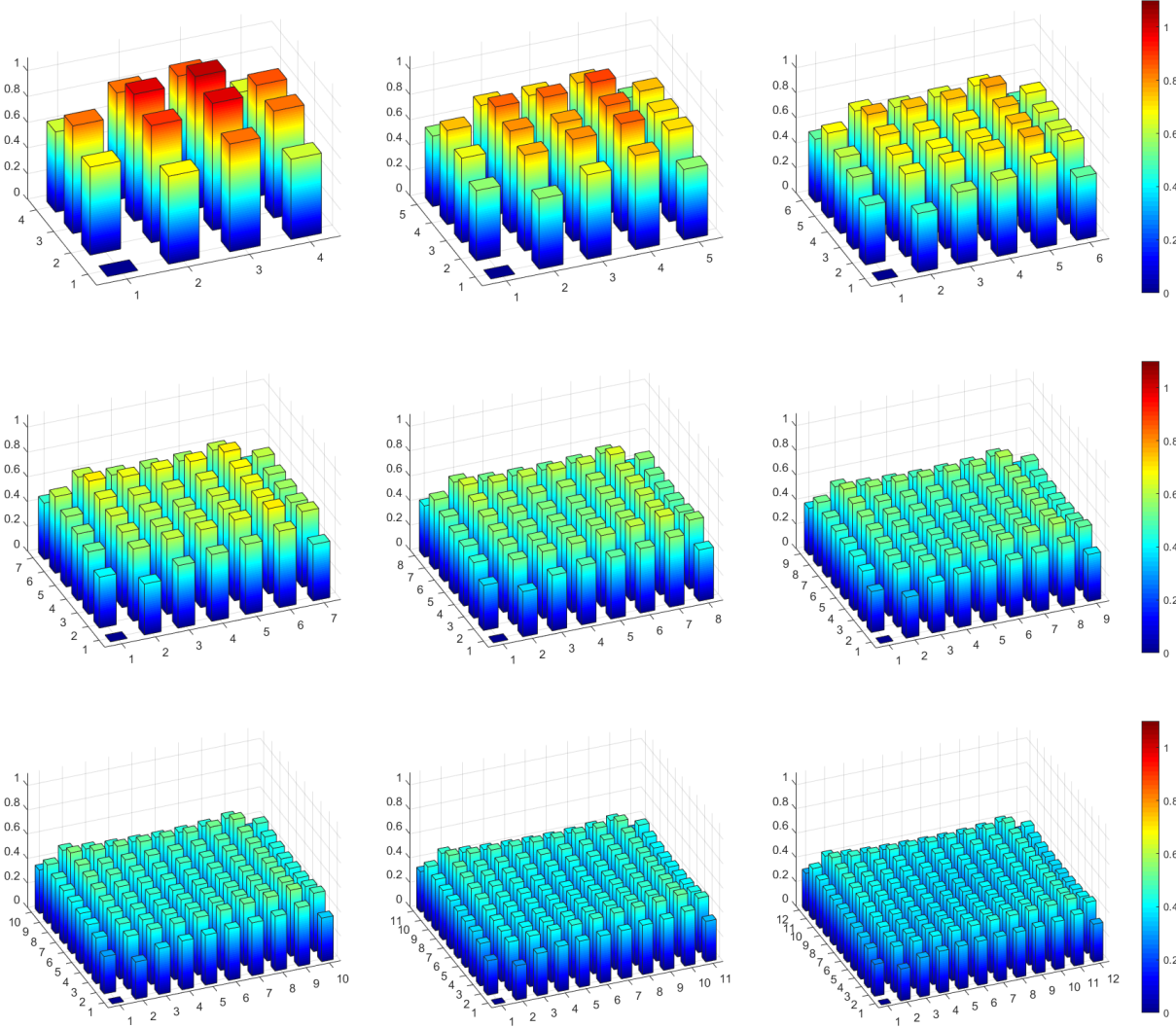


Figure 3.8: Spatial mean of maximum overloads relative to the initial overload on the closing valve metric displayed for the different nodes of the  $n = 3$  to  $n = 11$  square lattice networks.

### 3.3.3 Spatiotemporal maximum overload reached in the entire network

The maximum overload reached in the entire network after closing the valve on a node is a good way to characterize the same node. In Figure 3.9 are displayed the histograms representing such metric in absolute value. It is evident that the farther the closing valve node is from the vertices, the lower the maximum overload reached in the network.

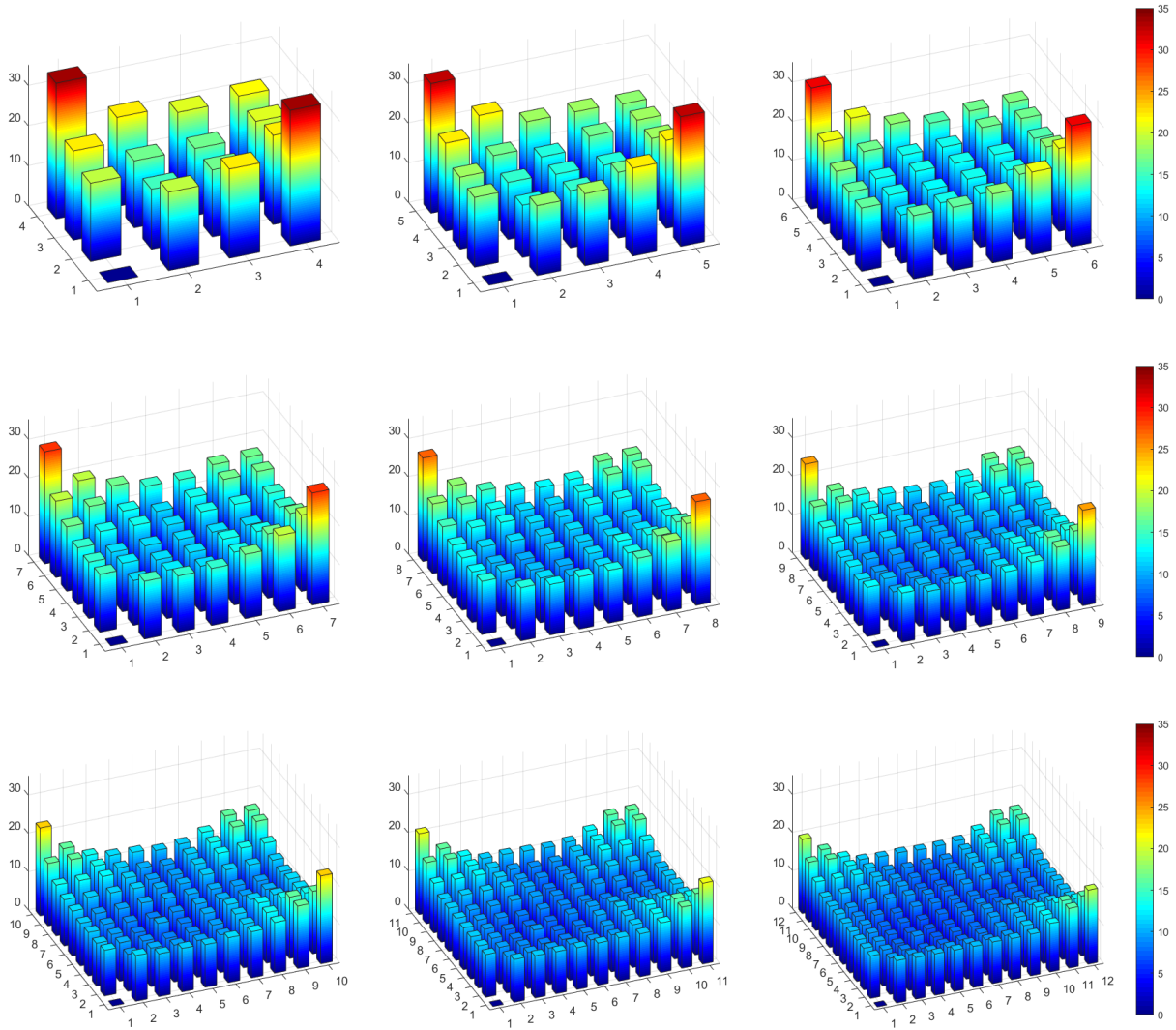


Figure 3.9: Spatiotemporal maximum overload metric displayed for the different nodes of the  $n = 3$  to  $n = 11$  square lattice networks. On the vertical axis, the overload is measured in  $m$ .

It could be informative to normalize the overall maximum with respect to the initial overload on the closing valve node. In this way, as displayed in Figure 3.10, one can visualize the nodes on which closing the valve leads to the higher relative maximum overload and whether this maximum is higher than the starting overload. For smaller networks, closing the valve on almost all the nodes leads to a maximum overload higher than the starting one. Increasing the size of the networks such maxima decrease in value for most of the nodes, except for the first internal nodes near the vertices, whose maximum/starting overload ratio remains constant.

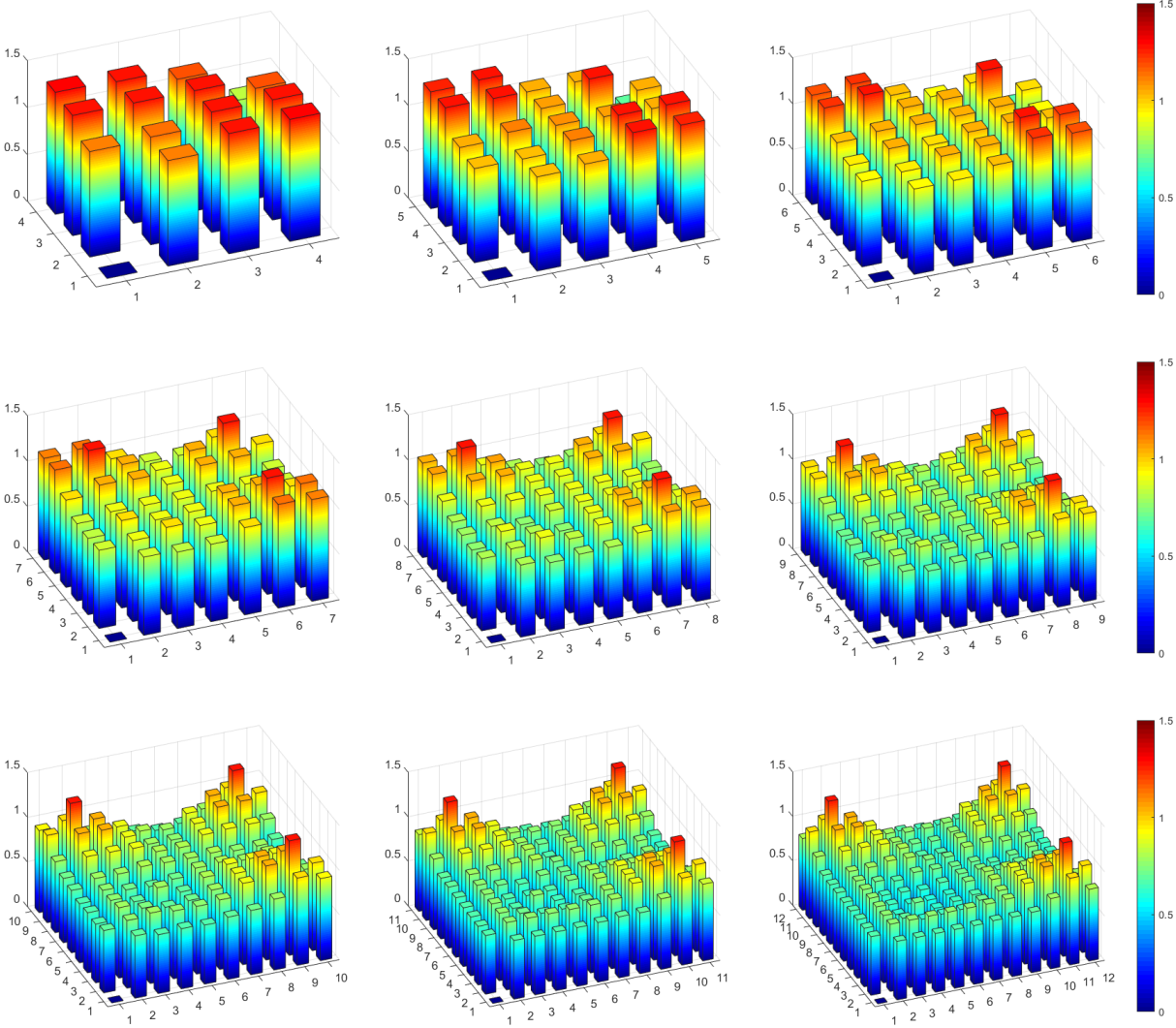


Figure 3.10: Spatiotemporal maximum overload relative to the initial overload on the closing valve node metric displayed for the different nodes of the  $n = 3$  to  $n = 11$  square lattice networks.

### 3.3.4 Distance between the closing valve node and the node in which the maximum overload is reached

The previous metrics don't give any information about the location of the maximum overload. In Figure 3.11 every closing valve node is associated to its distance (in terms of number of conduits) from the node in which the maximum overload is reached, normalized with respect to the diameter of the network, i.e. the maximum distance between two nodes ( $2n$ ).

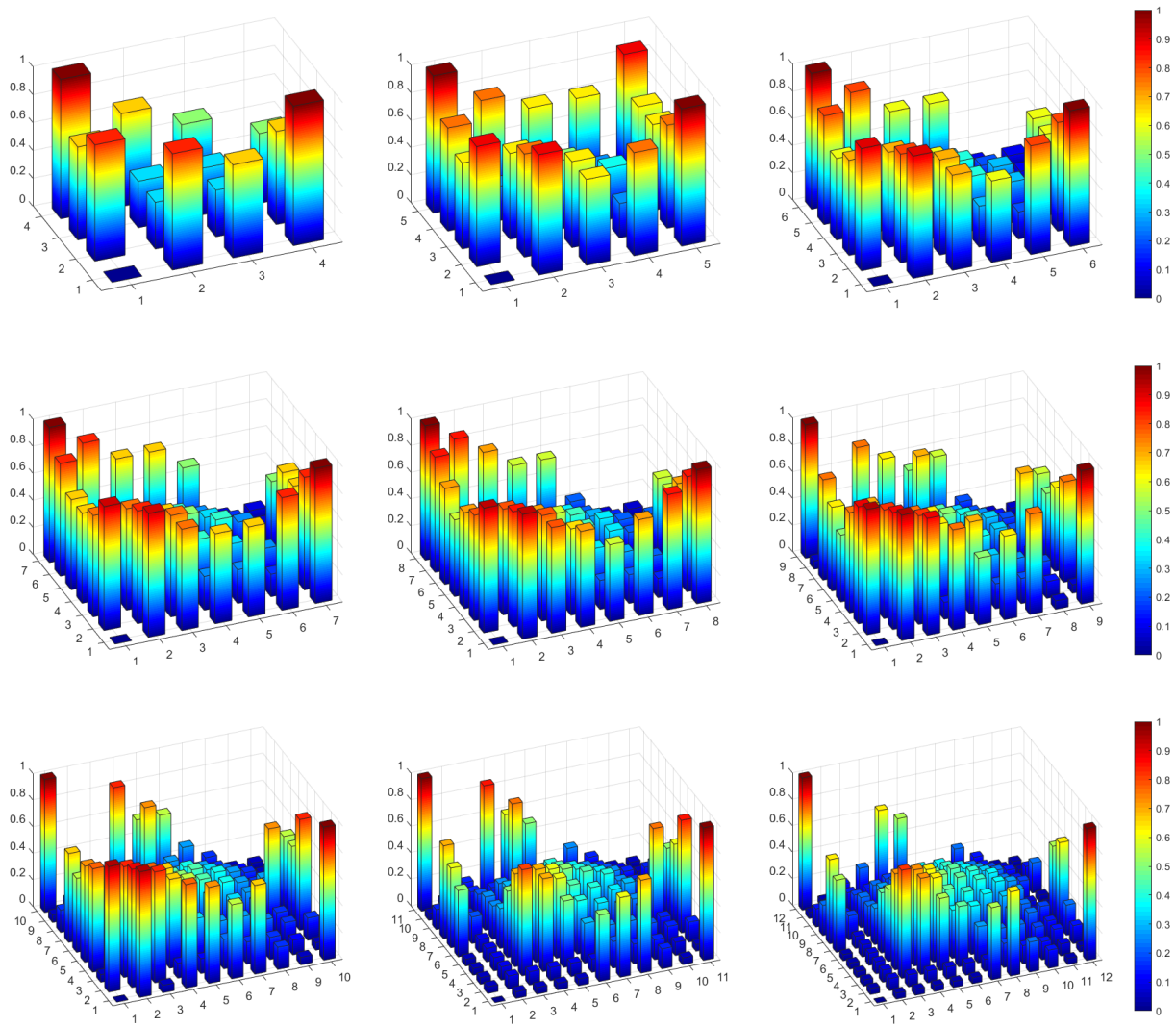


Figure 3.11: Distance from the closing valve node and the node in which the maximum overload is reached metric displayed for the different nodes of the  $n = 3$  to  $n = 11$  square lattice networks.

As hinted at the beginning of the chapter, there are cases in which the maximum overload is reached far from the closing valve node, even though the number of nodes for which this happens seems to decrease with the enlarging of the network.

Closing the valve on the vertices not opposite to the reservoir, the maximum is always reached on the other vertex, even though such maximum decreases in value with the enlarging of the network, as visible in Figure 3.9, becoming even lower than the starting overload on the closing valve. A different behaviour is registered for the internal nodes near the vertices: they keep a constant maximum overload changing the size of the network and such maximum is always reached near them (actually on the nearer vertex). In chapter 4 a simplified model for the propagation of pressure waves based on a network approach is developed in order to understand the underlying causes of these behaviours.

## 4. ATTEMPT TO A PREDICTIVE MODEL BASED ON NETWORK APPROACH

In this chapter a toy model of pressure wave propagation is developed, starting from a simplification of the characteristic equations, in order to understand the main mechanisms underlying the phenomenon. For computational simplicity and clarity of exposition, a square lattice hydraulic network with  $n = 3$  conduits per side is taken as example.

### 4.1 Simplification of the equations

#### 4.1.1 Wave branching at a junction

To understand how pressure waves behave when encountering a junction of multiple conduits, let's consider again the case of a node with  $n$  converging and  $m$  diverging conduits. Suppose that a pressure,  $\Delta H$ , and a discharge,  $\Delta Q$ , waves travel for the first time through a converging (or diverging) conduit and reaches node  $k$ . Suppose the initial head on the node is  $H_0$ . Neglecting the presence of the valve, the discharges before the arriving of the waves satisfy

$$\sum_{i=1}^n Q_i = \sum_{j=n+1}^{n+m} Q_j. \quad (4.1)$$

Neglecting dissipative effects, Equation (2.30) reads

$$\begin{aligned} H' &= \frac{\sum_{i=1}^n C_{p_i} - \sum_{j=n+1}^{n+m} C_{n_j}}{nn_k C_a} = \\ &= \frac{\sum_{i=1}^n Q_i - \sum_{j=n+1}^{n+m} Q_j \pm \Delta Q + C_a \Delta H + nn_k C_a H_0}{nn_k C_a} = \\ &= \frac{\pm \Delta Q + C_a \Delta H}{nn_k C_a} + H_0, \end{aligned}$$

so that the overload on the node is

$$\Delta H' = \frac{1}{nn_k} \left( \frac{\pm \Delta Q}{C_a} + \Delta H \right), \quad (4.2)$$

where the plus or minus sign in front of  $\Delta Q$  depends on the discharge wave coming from a converging or diverging conduit, respectively.

The discharge and head perturbations  $\Delta Q$  and  $\Delta H$  are related. In fact, using Equation (2.13), one finds

$$\Delta Q = \pm C_a \Delta H. \quad (4.3)$$

In this way, the overload reached at the node  $k$  is

$$\Delta H' = \frac{2}{nn_k} \Delta H, \quad (4.4)$$

which means that the pressure wave characterized by the overload  $\Delta H$ , once it reaches node  $k$  with  $nn_k$  nearest neighbors, is reduced by a factor  $f_k = \frac{2}{nn_k}$ .

The validity of such derivation is limited by the fact that the wave is propagating through this conduit for the first time. If the pressure wave already passed through such conduit, Equation (4.3) wouldn't be valid, but it should depend also on the overload previously reached at that node,  $\Delta \tilde{H}$ :

$$\Delta Q = \pm C_a (\Delta H - \Delta \tilde{H}). \quad (4.5)$$

#### 4.1.2 Wave reflection at a reservoir

Let's see what happens to a wave reflected by the reservoir. Consider a reservoir connected by a pipeline to a junction of  $m$  conduits. Suppose that a wave  $\Delta \tilde{H}$  propagates from the junction towards the reservoir. At the reservoir the head is brought back to its initial level, so there's no overload propagating back through the conduit,  $\Delta H = 0$  but, using Equation (4.4),  $\Delta Q = \mp C_a \Delta \tilde{H}$ . So Equation (4.2) for the overload on the junction once the wave returns from the reservoir becomes

$$\Delta H' = -\frac{1}{m} \Delta \tilde{H} = -\frac{1}{2} \frac{2}{m} \Delta \tilde{H}, \quad (4.6)$$

so that, maintaining the reduction factor of the  $m$ -conduits junction as  $\frac{2}{m}$ , we can assign to the reservoir nodes an effective reduction factor  $f_r = -\frac{1}{2}$  (notice that this is just a convenience, since the overload at the reservoir node is not actually  $-\frac{1}{2} \Delta \tilde{H}$ , but it doesn't matter because we know that at the reservoir nodes the overload is always null). Such derivation works even for subsequent passages of the wave, since the reservoir head level is always re-established in the conduit.

## 4.2 Overloads computation according to the predictive model

We associated the hydraulic network to an undirected (waves can travel in both directions in a conduit) and unweighted (all conduits share the same structural properties) graph  $G = (V, E)$ , represented in Figure 4.1. Both edges ( $E$ ) and nodes ( $V$ ) in the graph mirror, respectively, the conduits and the junctions in the hydraulic network, except for the reservoir, which is represented by as many nodes as the number of conduits attached to it. In our case of a square lattice with  $n$  conduits per side and with a reservoir in a vertex, it is represented by node 1 connected to node 2 and node  $(n + 1)^2 + 1 = 17$  connected to node  $n + 2 = 5$ .

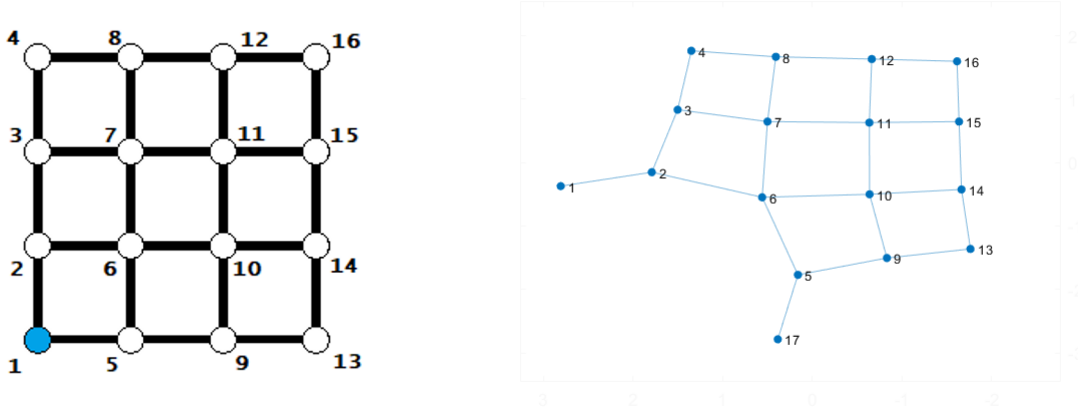


Figure 4.1: Hydraulic network (left) and its graph representation used for topological analysis (right).

To each node we assigned a *reduction factor*:

$$f_k = \frac{2}{nn_k}, \quad k \in \{2, \dots, 16\} \quad (4.7)$$

$$f_1 = f_{17} = -\frac{1}{2}. \quad (4.8)$$

Then, for each couple of nodes we computed all the paths connecting the two nodes up to a maximum length  $l_{max}$ , since in principle there are infinite paths connecting two nodes. As previously explained, we don't consider paths of the type  $p = [\dots, i, j, i, \dots], \forall i, j \notin \{1, (n + 1)^2 + 1\}$  since the ways pressure and discharge waves are reflected in these cases is too complex to be condensed in reduction factors assigned to nodes. We call paths along which we can compute the wave propagation as *direct*.

The idea is to compute the overload reached on node  $j$  at time  $t = t_0 + l\frac{L}{a}$  after closing the valve on node  $s$  at time  $t = t_0$  as the superposition of all the waves traveling along *direct* paths of  $l$  conduits. The amplitude of a wave that travels along a path will be reduced at every node encountered by the multiplicative reduction factor in Equations (4.7) and (4.8).

For example, let's consider the first overload reached on node  $j = 16$  if a unitary pressure wave is generated on node  $s = 9$ . There are 4 paths of length  $l = 4$  connecting nodes 9 and 16, which are represented in Figure 4.2:

$$p_A = [9 \quad 13 \quad 14 \quad 15 \quad 16]$$

$$p_B = [9 \quad 10 \quad 14 \quad 15 \quad 16]$$

$$p_C = [9 \quad 10 \quad 11 \quad 15 \quad 16]$$

$$p_D = [9 \quad 10 \quad 11 \quad 12 \quad 16].$$

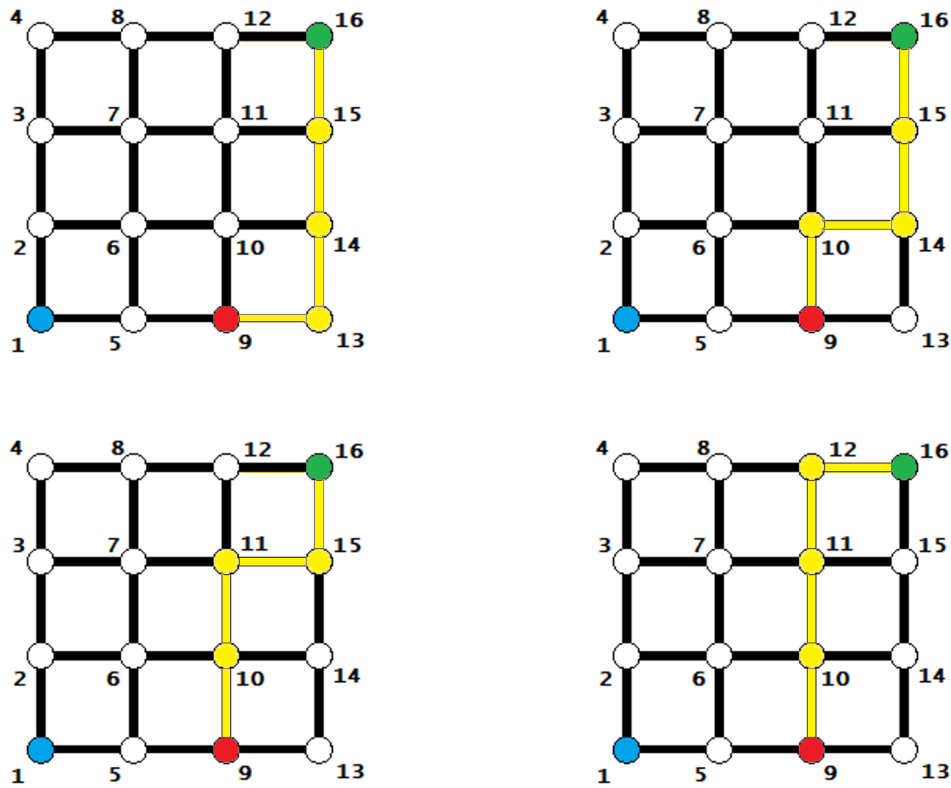


Figure 4.2: From left to right, from up to bottom, representation of the four paths  $p_A$ ,  $p_B$ ,  $p_C$  and  $p_D$  of length  $l = 4$  that connect node 9 (red) to node 16 (green).

The waves propagating through these different paths give

$$\Delta H_{16}^A = f_{13} \cdot f_{14} \cdot f_{15} \cdot f_{16} = 1 \cdot \frac{2}{3} \cdot \frac{2}{3} \cdot 1 = \frac{4}{9},$$

$$\Delta H_{16}^B = f_{10} \cdot f_{14} \cdot f_{15} \cdot f_{16} = \frac{1}{2} \cdot \frac{2}{3} \cdot \frac{2}{3} \cdot 1 = \frac{2}{9},$$

$$\Delta H_{16}^C = f_{10} \cdot f_{11} \cdot f_{15} \cdot f_{16} = \frac{1}{2} \cdot \frac{1}{2} \cdot \frac{2}{3} \cdot 1 = \frac{1}{6},$$

$$\Delta H_{16}^D = f_{10} \cdot f_{11} \cdot f_{12} \cdot f_{16} = \frac{1}{2} \cdot \frac{1}{2} \cdot \frac{2}{3} \cdot 1 = \frac{1}{6}.$$

The first overload reached on node  $j = 16$  has, then, unitary amplitude:

$$\Delta H_{16} = \Delta H_{16}^A + \Delta H_{16}^B + \Delta H_{16}^C + \Delta H_{16}^D = \frac{4}{9} + \frac{2}{9} + \frac{1}{6} + \frac{1}{6} = 1.$$

In this examples, waves traveling through all the paths can be computed by the model because there's no path passing through the same conduit consecutively twice or more times. Actually, we can compute waves through all the paths, connecting the starting and ending nodes, *if and only if* such paths are shortest paths, i.e. we can only compute with a certain precision the first overload reached on each node. In the previous example, if we consider the paths of length  $l = 6$  between nodes 9 and 16, there are many paths that present the same conduit consecutively twice, for example path [9 5 9 10 11 12 16], and even thrice, for example path [9 10 9 10 11 12 16] (Figure 4.3).

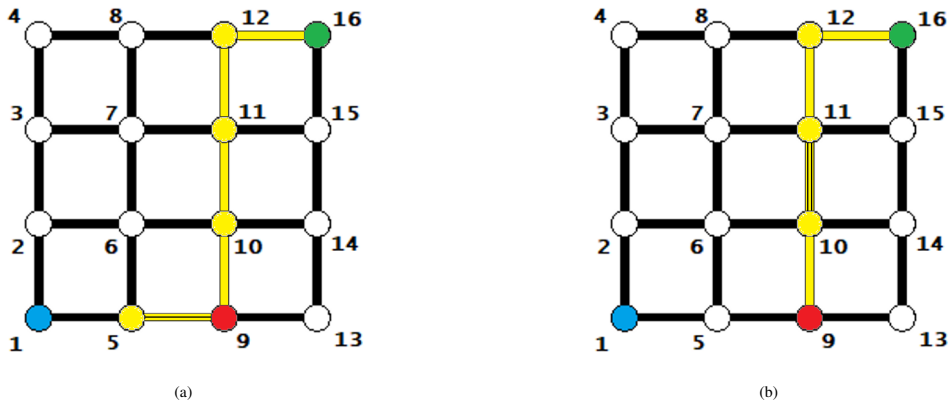


Figure 4.3: Examples of paths of length  $l = 6$  between nodes 9 (red) and 16 (green), passing consecutively through the same conduit twice (a), [9 5 9 10 11 12 16], and thrice (b), [9 10 9 10 11 12 16]. The number of yellow stripes in a conduit indicates the number of times it is traveled.

Furthermore, it can be shown that waves that pass consecutively through the same conduit twice have their amplitude reduced more than if it was computed with the simplified reduction factors of the model, but it would still be non-negative. Instead, waves passing consecutively through a conduit thrice have their amplitude become negative often (actually always, if there's no dead end conduit).

As an example, in Figure 4.4 is plotted the temporal evolution of overload on node 16 after closing the valve on node 9 at 0.5s. The first overload is predicted with a light error, but the model fails to estimate subsequent overloads, due to the absence in the model of negative waves coming from paths that pass through the same conduit thrice or more times.

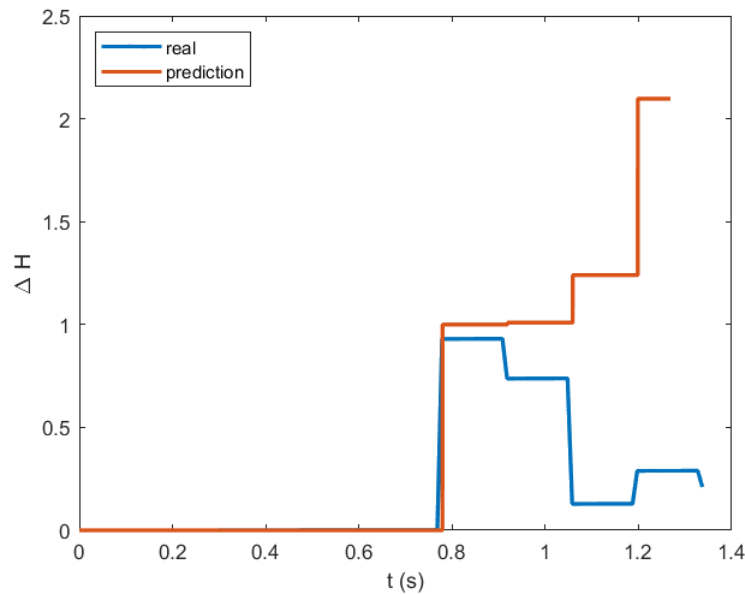


Figure 4.4: Overload time evolution on node 16 after closing

Modelization of reflected waves would be an interesting task, that we'll leave to future studies. We want to focus now on the first overloads reached on each node, to understand the possibilities and the limits of this toy model.

### 4.3 Wave factors correction to include dissipation effects

Since the first overloads reached in the network appear to be the only ones for which the model works well, let's improve the prediction by introducing a general correction factor  $\eta$  multiplying the reduction factors, that accounts *a posteriori* for dissipation effects. The first overload reached on a node at distance  $l$  from the closing valve node, that is superposition of many waves travelling through the different paths, is then reduced by a factor  $\eta^l$ . In this theoretical frame, the relative error made using no correction factor would be

$$\varepsilon_{th} = \frac{(1 - \eta^l)\Delta H}{\eta^l \Delta H} = \eta^{-l} - 1. \quad (4.9)$$

In Figure 4.5 such relative errors, obtained comparing the model predictions without correction factor  $\eta$  and the simulation data, are plotted against the length of the shortest paths between the closing valve node and the node on which the overload is measured. Fitting the formula in Equation (4.9) to the data, we obtained an optimal value  $\eta^* = 0.9845$ .

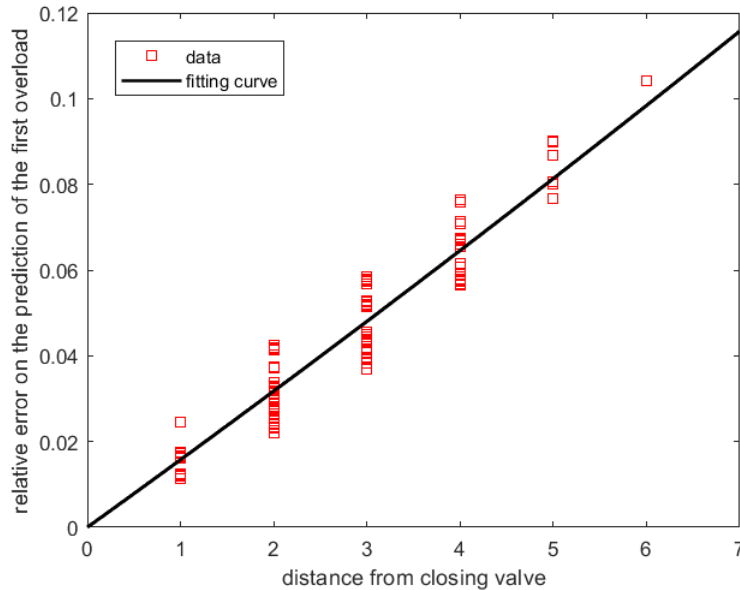


Figure 4.5: The relative error made in predicting the first overload reached on a certain node of the network is plotted against the length of the shortest paths between the closing valve node and the node on which the overload is measured. The red squares are the data derived from simulations and the black curve is the theoretical curve expressed in Equation (4.9) fitting the data.

In Figure 4.6 the mean error with its standard deviation is plotted against different values of the correction factor  $\eta$ . The minimal value of  $\eta$  coincides with the one obtained previously and the mean relative error in this case is  $\langle \varepsilon \rangle = 0.005$ , so in the corrected model an average percentage error of 0.5% is made when predicting the first overloads reached in the network, compared to the 4% percentage error made without any correction, i.e.  $\eta = 1$ .

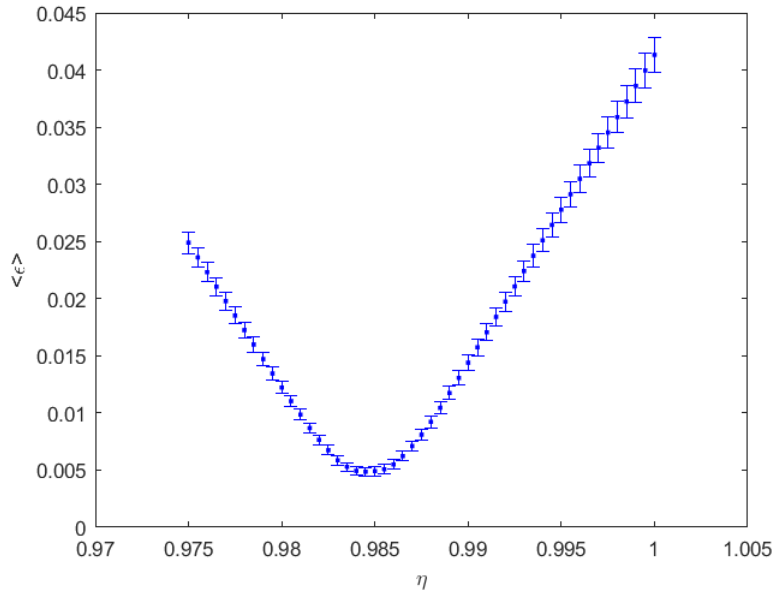


Figure 4.6: Average relative error made by the model when predicting the first overloads reached on the different nodes of the network as a function of the correction factor  $\eta$ . The rightmost point, relative to  $\eta = 1$  is the average relative error made without any correction. The minimum of the curve corresponds to the optimal value of  $\eta$  already obtained with the data fitting.

Further studies on networks with a different topology and different structural properties, will be necessary to validate this modelization of dissipation effects in the propagation of pressure waves.

## 4.4 Average delay and max-first connections

In Figure 4.7 the delay, in terms of difference between the length of the shortest paths and the length of the paths that bring the maximal wave from the closing valve node to the node we're interested in, is plotted against the different closing valve nodes' location. It is evident how central nodes in the network present a higher average delay than those nodes on the borders. We then expect that prediction for central nodes could be difficult.

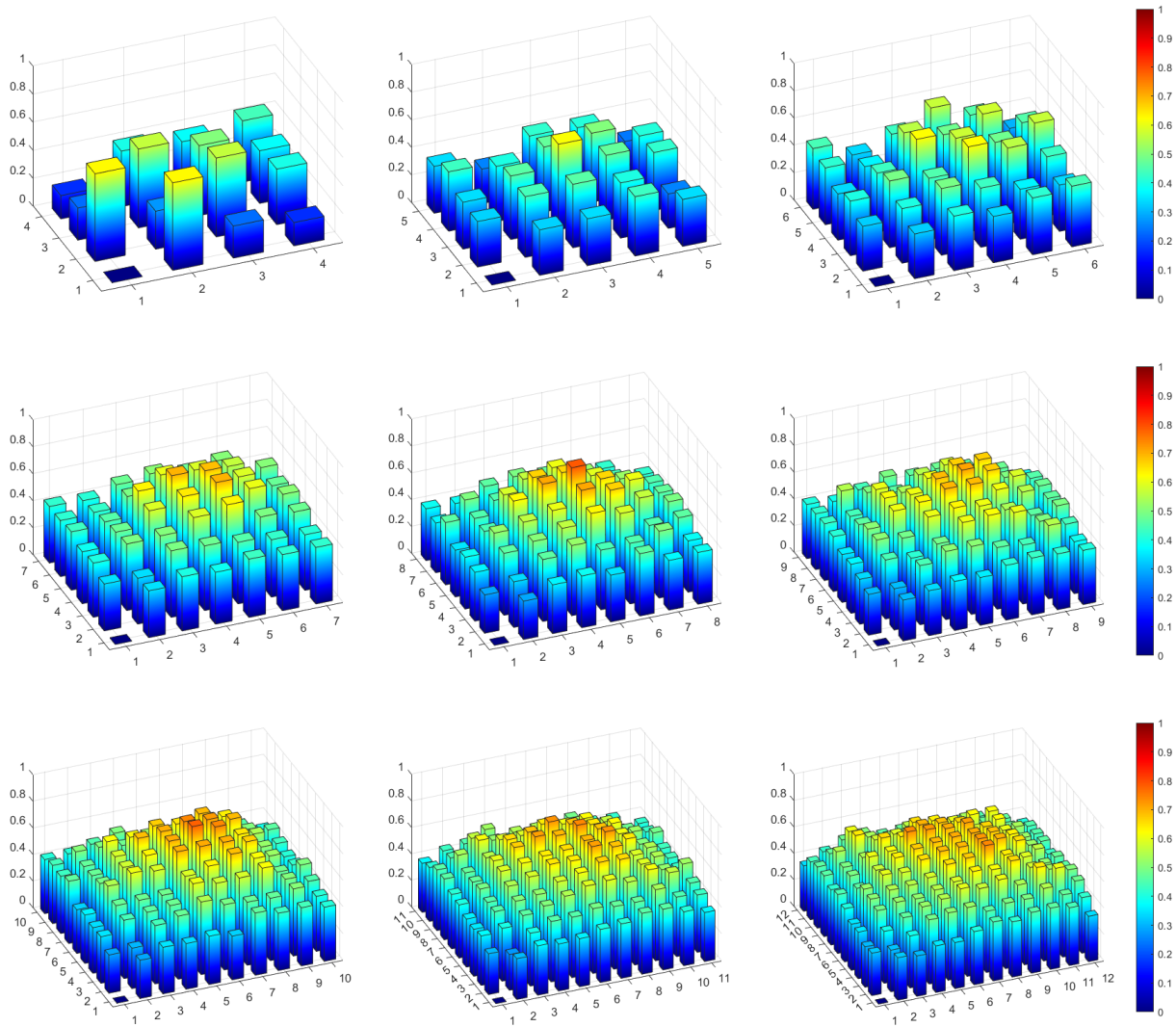


Figure 4.7: Spatial mean of delay between the first arrival of the waves and the actual maximum (in terms of difference in the number of conduits between the shortest path and the length of paths that bring the maximal wave) as a function of the closing valve node position.

The increasing of the average delay as one considers more and more internal nodes may be due to the fact that central nodes begin to have paths starting from them that travel along the borders and through vertices late: this, combined with the higher number of paths with respect to more peripheral nodes, could lead to a greater amplification of the waves at later times.

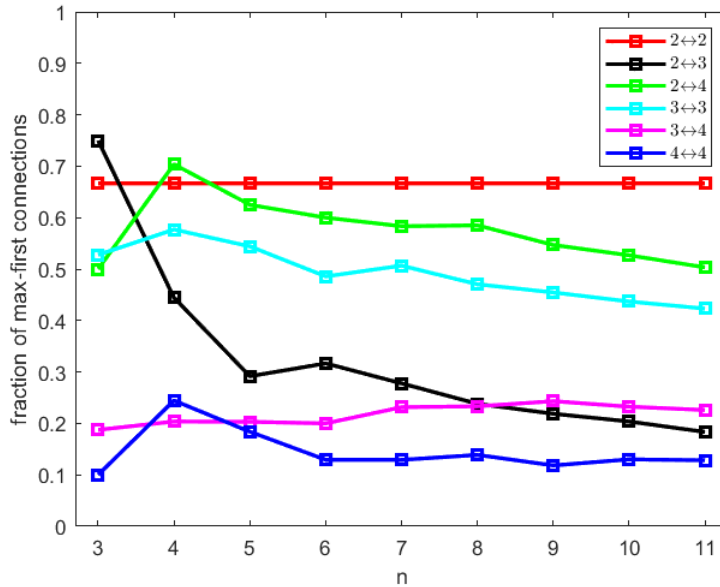


Figure 4.8: Max-first connections for nodes with different number of nearest neighbors.

The last analysis is a topological categorization of *max-first connections*, i.e. couples of nodes such that closing the valve on one node the maximum overload on the other is reached at the first arrival of the wave, done taking into account the number of nearest neighbors of the two nodes. In Figure 4.8 the fraction of max-first connections that involve nodes with different number of nearest neighbors are plotted for increasing size of the network. Apart from adjustments for smaller networks, from  $n = 6$  on it seems that these fractions remain stable, maybe some are slowly decreasing but studies on larger networks would be necessary to understand the trend. The  $2 \leftrightarrow 2$  max-first fraction is constant, because there are always 3 of such nodes. Studies on different type of networks will be useful to increase statistics on this fraction.

From this analysis, we can expect the predictive model on the  $n = 3$  network to work well for nodes with fewer nearest neighbors.

## 5. PREDICTION RESULTS

In this chapter the predictive power and the limits of the model are tested on the  $n = 3$  square lattice network.

Since the first overloads reached on each node can be predicted with precision, let's see whether using them as a prediction for the maximum overloads is a fair choice. Let's analyze the performances of this predictive model for different locations of the closing valve node.

Results are not presented for every node, since there is a symmetry with respect to the diagonal passing through the reservoir, so that results can be mirrored with respect to this line.

# 5.1 Closing valve on node 16 (4,4)

In Figure 5.1 are shown the real and predicted maximum overloads reached on each node after closing the valve in (4,4) (node 16) and the relative error made. In this case the predictive model works pretty well, especially on internal nodes and the borders opposite to the closing valve node, but it makes a percentage error up to 20% on the other vertices.

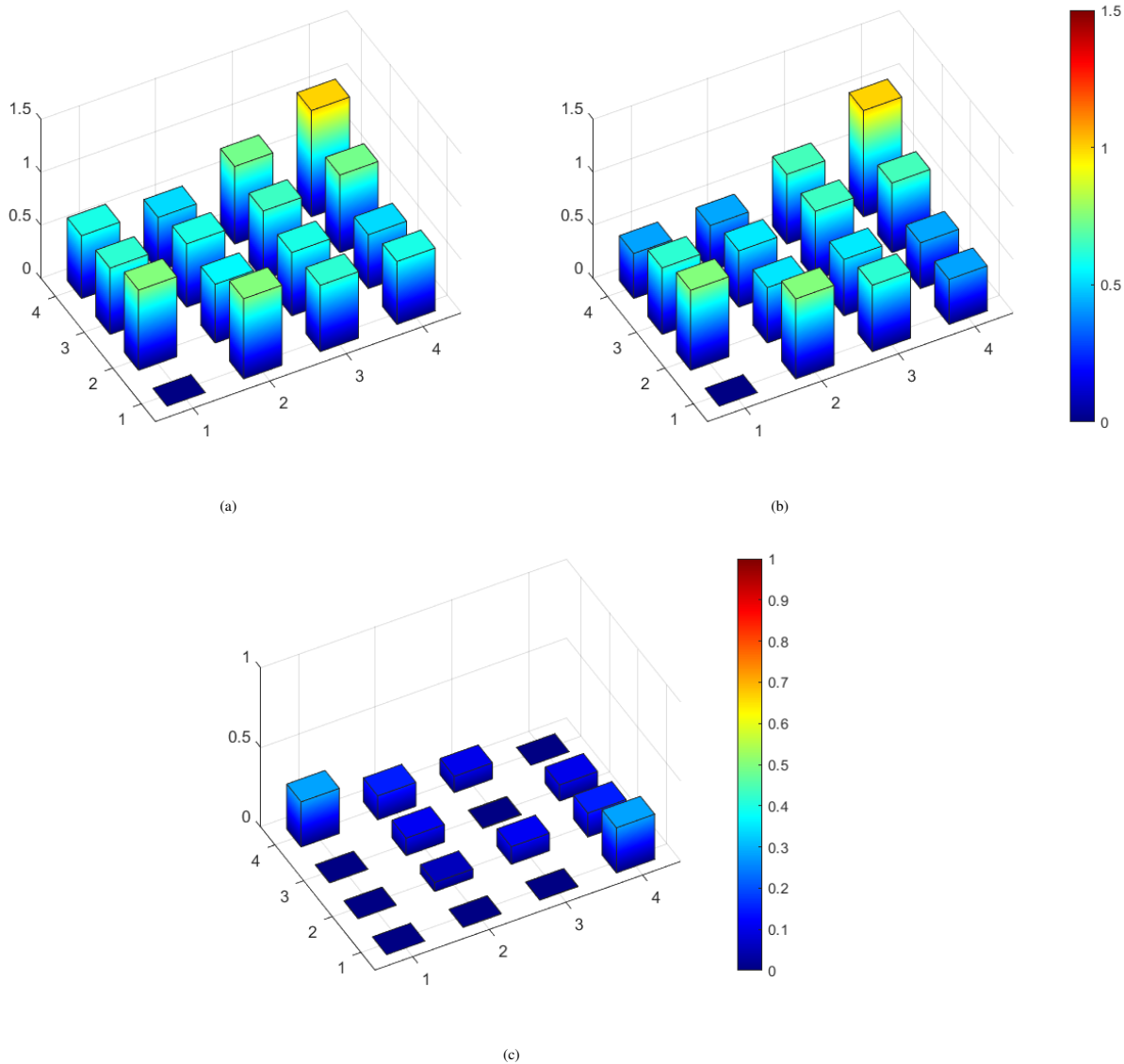


Figure 5.1: (a) Maximum overloads reached on each node closing the valve on node 16, that in these graphs is node (4,4). (b) Predictions using the first overloads reached at each node. (c) Percentage error made in the prediction on each node.

## 5.2 Closing valve on node 15 (4,3) (or specularly 12 (3,4))

In Figure 5.2 are displayed the histograms showing the real and predicted maximum overloads reached on each node after closing the valve in (4,3) (node 15) and the relative error made. In this case the predictive model works well on the borders, but not in the internal nodes and on side opposite to the closing valve node, especially in (1,3) (node 3), where the maximum overload of the entire network is reached.

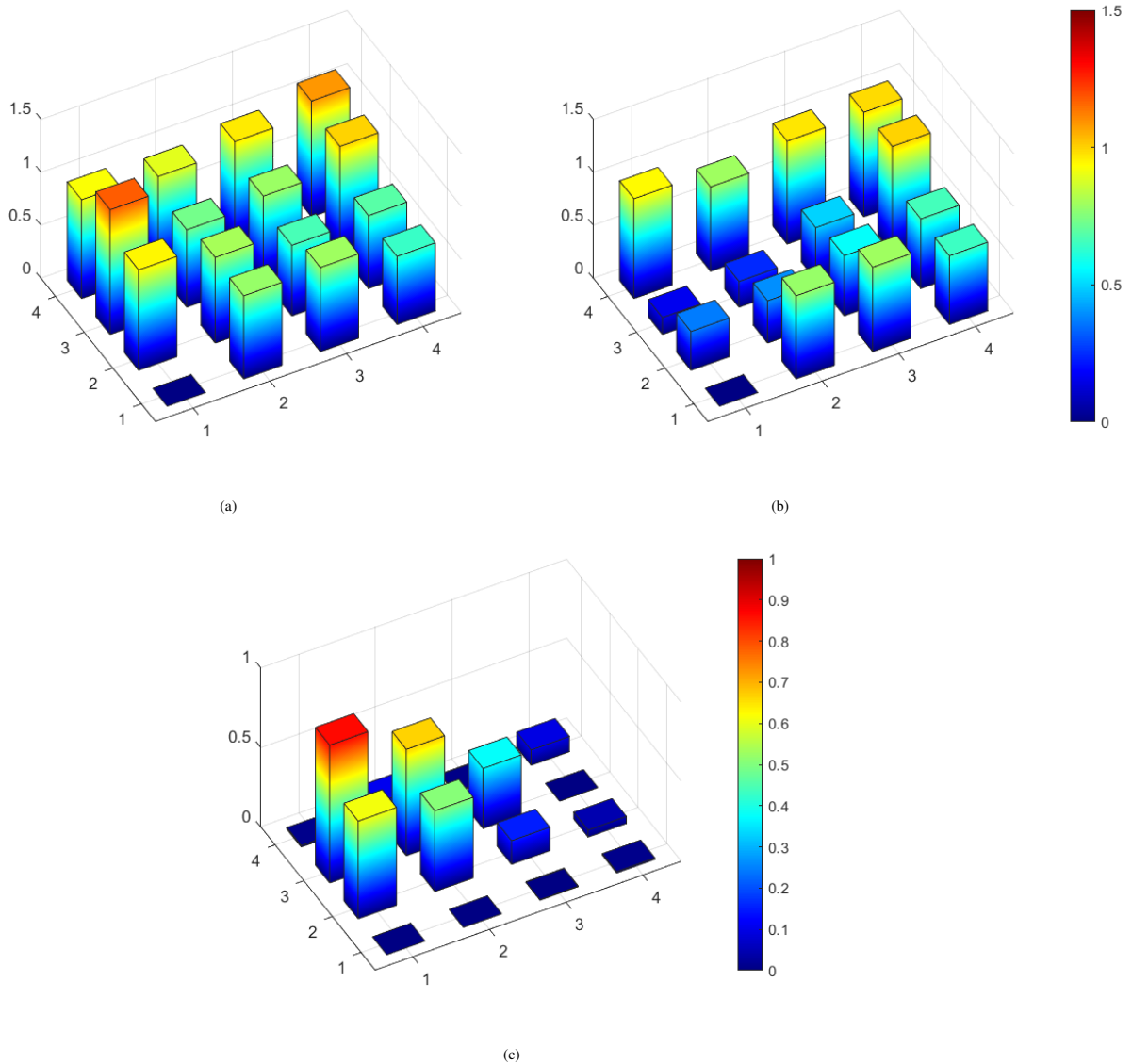


Figure 5.2: (a) Maximum overloads reached on each node closing the valve on node 15, that in these graphs is node (4,3). (b) Predictions using the first overloads reached at each node. (c) Percentage error made in the prediction on each node.

### 5.3 Closing valve on node 14 (4,2) (or specularly 8 (2,4))

In Figure 5.3 are displayed the histograms showing the real and predicted maximum overloads reached on each node after closing the valve in (4,2) (node 14) and the relative error made. As in the previous case, the predictive model on near borders works well, but on the opposite side and internal nodes the prediction fails, especially on the node (the same as before) in which the maximum is reached.

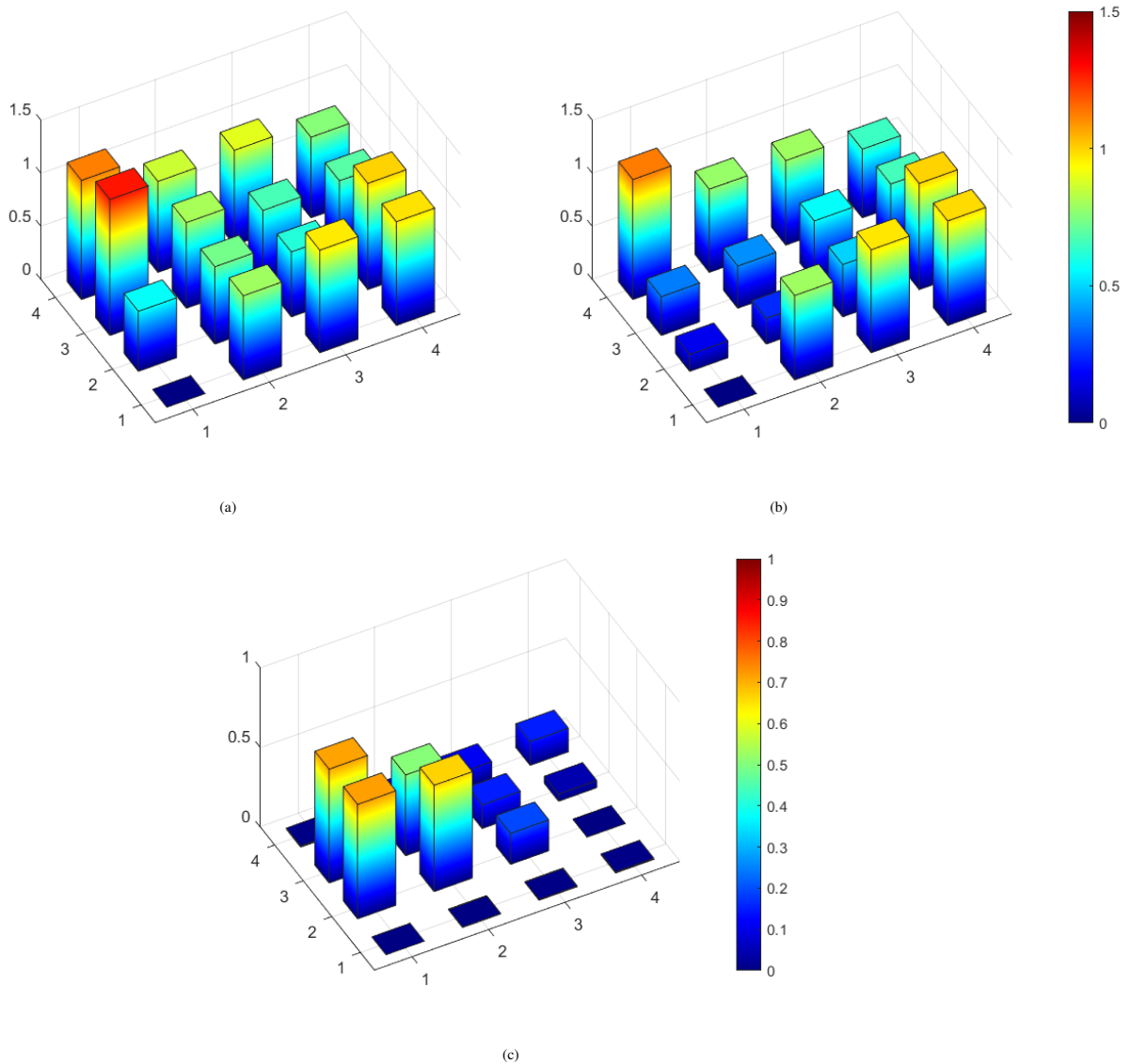


Figure 5.3: (a) Maximum overloads reached on each node closing the valve on node 14, that in these graphs is node (4,2). (b) Predictions using the first overloads reached at each node. (c) Percentage error made in the prediction on each node.

## 5.4 Closing valve on node 13 (4,1) (or specularly 4 (1,4))

In Figure 5.4 are displayed the histograms showing the real and predicted maximum overloads reached on each node after closing the valve in (4,1) (node 13) and the relative error made. The predictive model works really well on all nodes, except for light discrepancies. The maximum overload on the entire network is predicted. Results when closing the valve on node 4 in (1,4) are mirrored with respect to the diagonal passing through the reservoir.

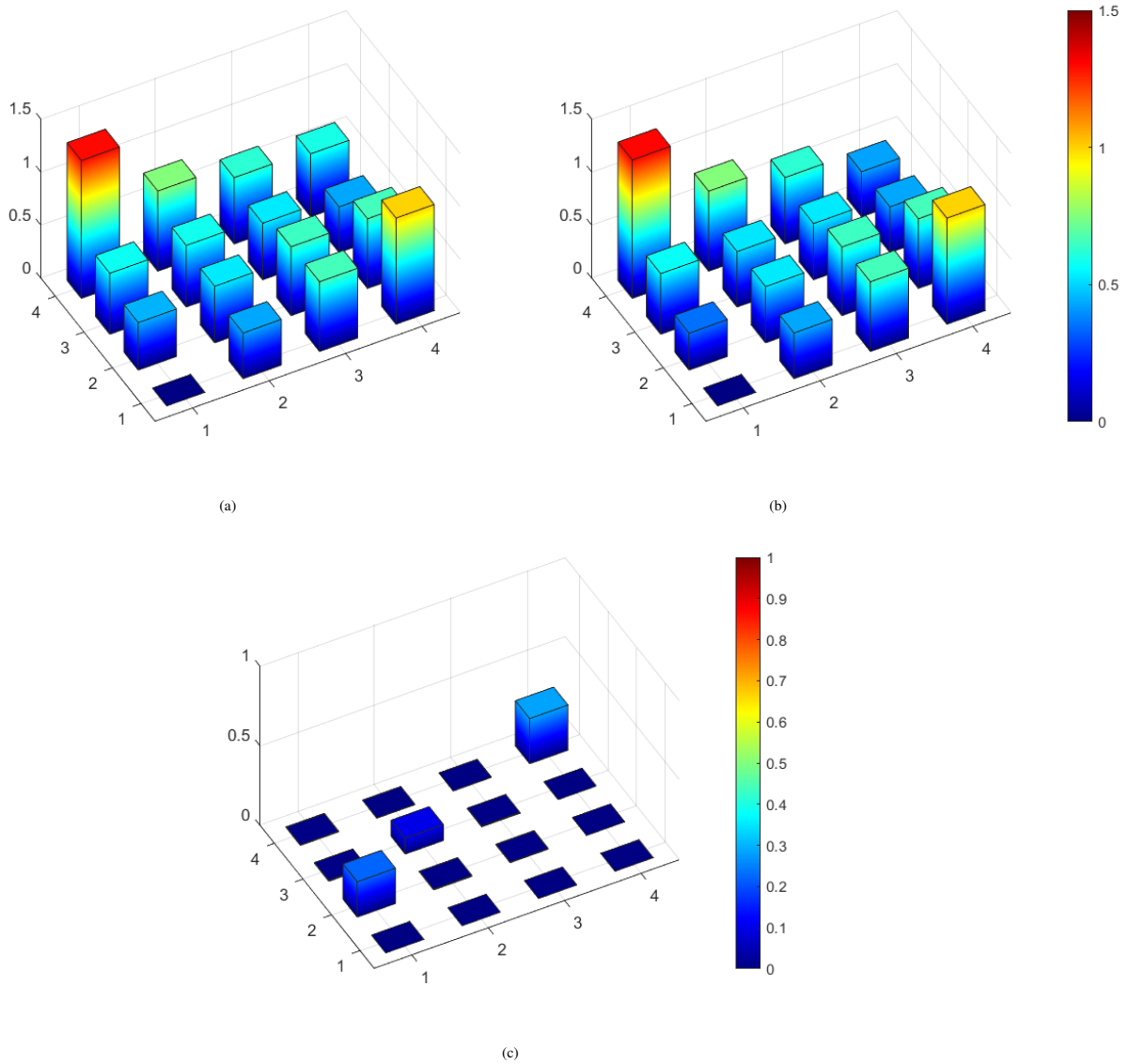


Figure 5.4: (a) Maximum overloads reached on each node closing the valve on node 13, that in these graphs is node (4,1). (b) Predictions using the first overloads reached at each node. (c) Percentage error made in the prediction on each node.

## 5.5 Closing valve on node 11 (3,3)

In Figure 5.5 are displayed the histograms showing the real and predicted maximum overloads reached on each node after closing the valve in (3,3) (node 11) and the relative error made. The performance of the predictive model is underwhelming, since it works well only on vertices. The maximum overload on the entire network on the vertex in (4,4) (node 16) is predicted, but similar critical overloads on the other internal nodes are missed by the model.

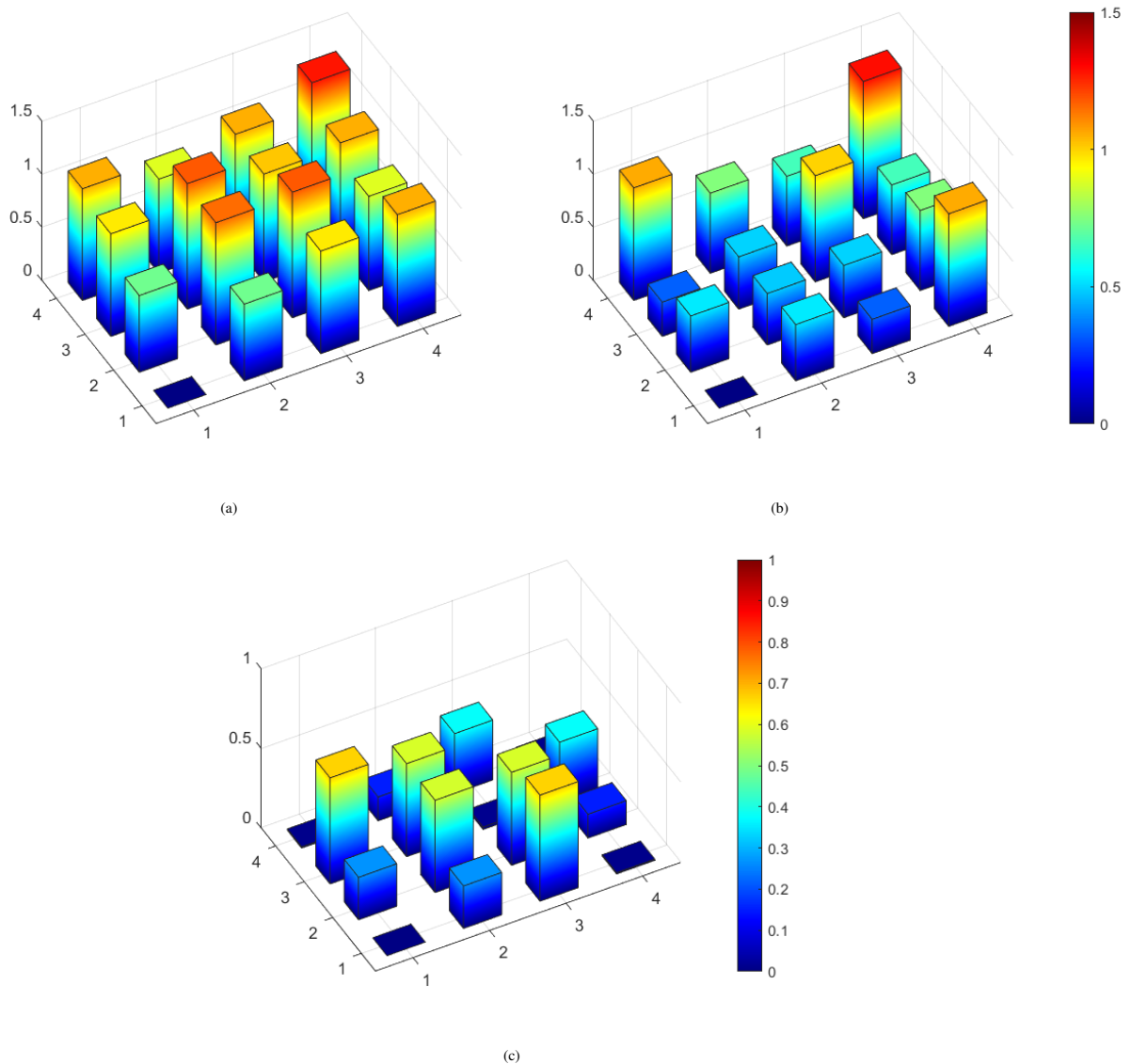


Figure 5.5: (a) Maximum overloads reached on each node closing the valve on node 11, that in these graphs is node (3,3). (b) Predictions using the first overloads reached at each node. (c) Percentage error made in the prediction on each node.

## 5.6 Closing valve on node 10 (3,2) (or specularly 7 (2,3))

In Figure 5.6 are displayed the histograms showing the real and predicted maximum overloads reached on each node after closing the valve in (3,2) (node 10) and the relative error made. The predictive model works well on border near the closing valve node and vertices, but not on the other internal nodes and the farther borders. The maximum overload on the vertex in (4,1) (node 13) is predicted.

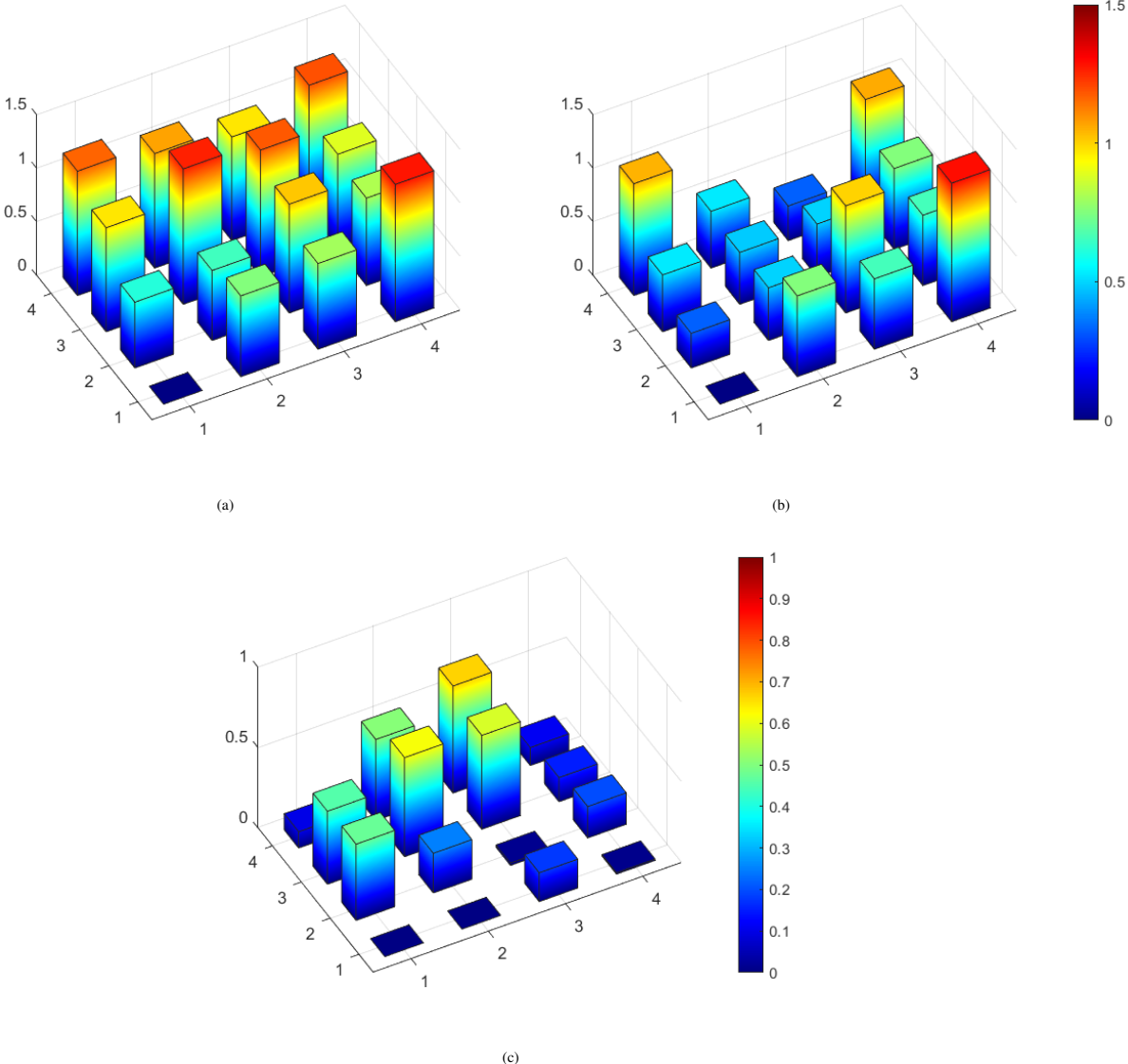


Figure 5.6: (a) Maximum overloads reached on each node closing the valve on node 10, that in these graphs is node (3,2). (b) Predictions using the first overloads reached at each node. (c) Percentage error made in the prediction on each node.

## 5.7 Closing valve on node 9 (3,1) (or specularly 3 (1,3))

In Figure 5.7 are displayed the histograms showing the real and predicted maximum overloads reached on each node after closing the valve in (3,1) (node 9) and the relative error made. The performance is low on the opposite side of the network with respect to the closing valve node, where the maximum is reached, on the farthest internal nodes and even on some nodes on the other border connected to the reservoir.

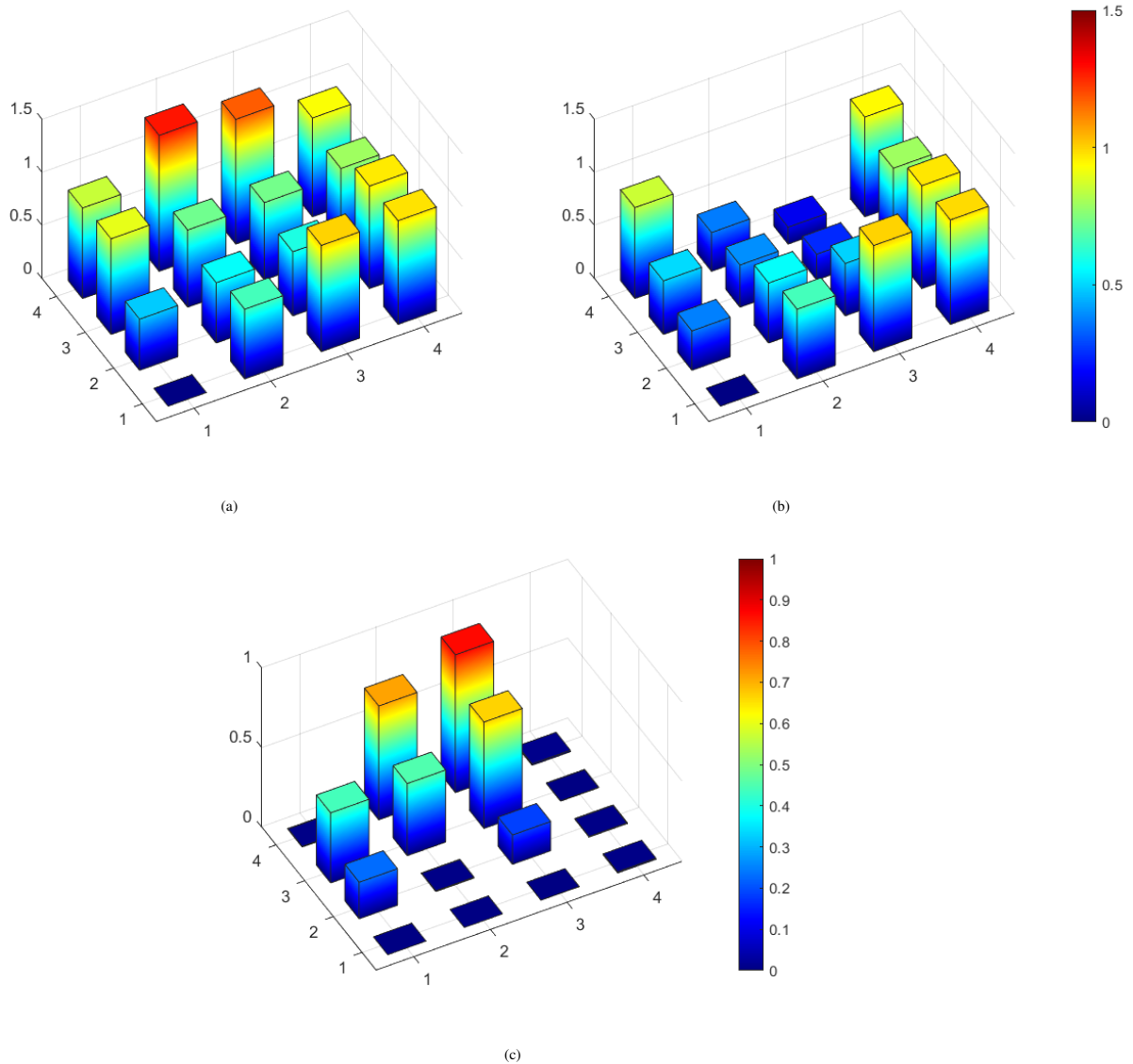


Figure 5.7: (a) Maximum overloads reached on each node closing the valve on node 9, that in these graphs is node (3,1). (b) Predictions using the first overloads reached at each node. (c) Percentage error made in the prediction on each node.

## 5.8 Closing valve on node 6 (2,2)

In Figure 5.8 are displayed the histograms showing the real and predicted maximum overloads reached on each node after closing the valve in (2,2) (node 6) and the relative error made. The maximum overloads reached on the borders including the reservoir and on vertices are well predicted, whereas the other maximum overloads are not, especially that in (3,3), that is node 11, which is the maximum in the entire network.

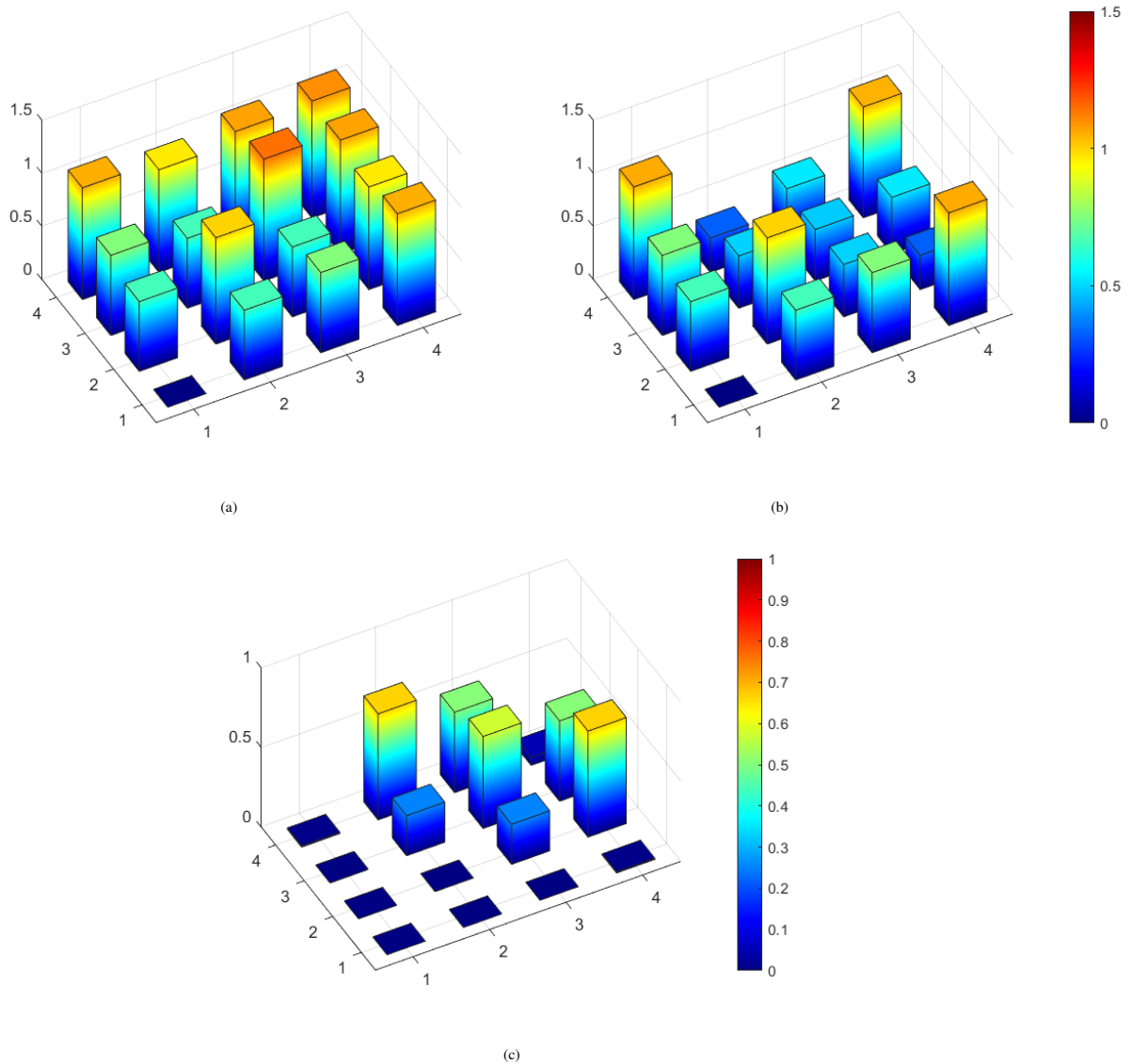


Figure 5.8: (a) Maximum overloads reached on each node closing the valve on node 6, that in these graphs is node (2, 2). (b) Predictions using the first overloads reached at each node. (c) Percentage error made in the prediction on each node.

## 5.9 Closing valve on node 5 (2,1) (or specularly 2 (1,3))

In Figure 5.9 are displayed the histograms showing the real and predicted maximum overloads reached on each node after closing the valve in (2,1) (node 5) and the relative error made. The model doesn't work on the opposite side of the network. However the maximum is predicted, since it is reached on the vertex opposite to the reservoir.

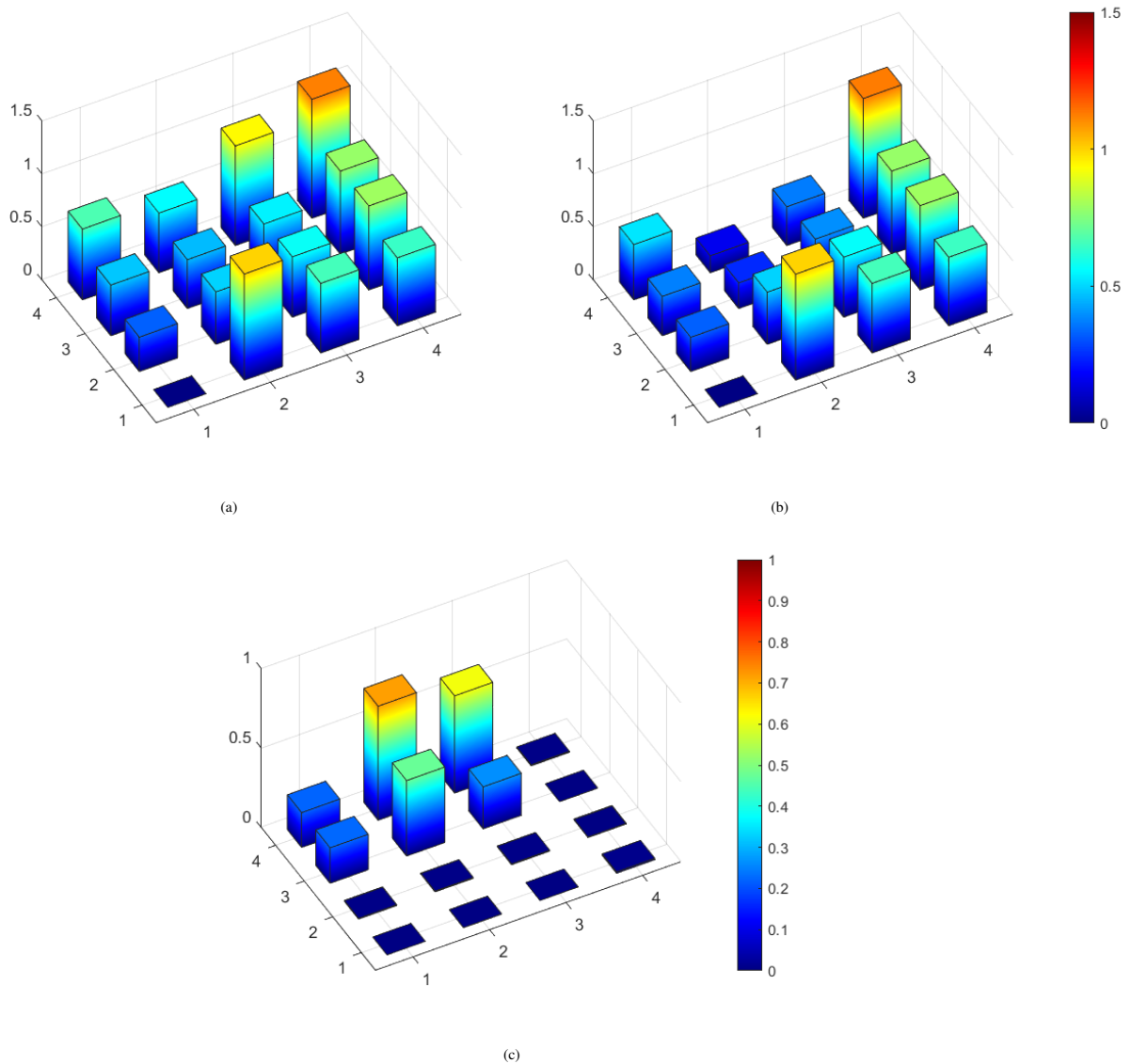


Figure 5.9: (a) Maximum overloads reached on each node closing the valve on node 5, that in these graphs is node (2, 1). (b) Predictions using the first overloads reached at each node. (c) Percentage error made in the prediction on each node.

## 5.10 Global results

In Figure 5.10 is reported a scheme of the hydraulic network in which nodes are colored in green or red if, closing the valve on them, the model can or can't predict on which node the maximum overload is reached.

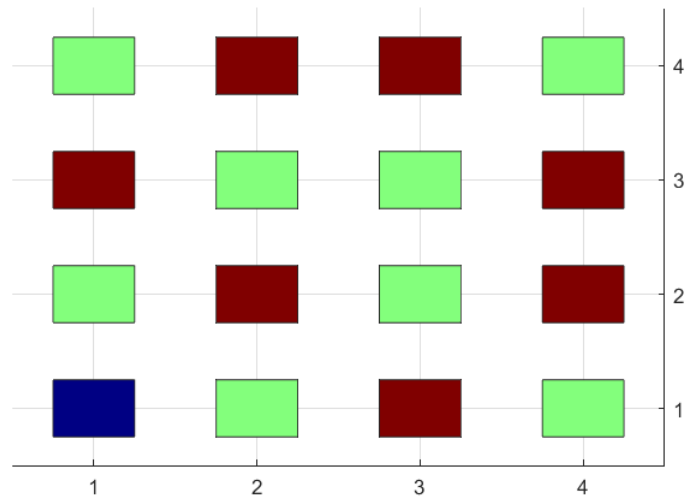


Figure 5.10: Scheme of the nodes for which, closing the valve on them, the location of the maximum overload is (green) or isn't (red) predicted right by the model.

Border nodes far from the reservoir and internal nodes near the reservoir seem to be the ones for which, closing the valves on them, the maximum overload on the entire network cannot be predicted by the model.

In Figure 5.11 the metric that associates each node to the maximum relative overload reached in the entire network after the closing of its valve, described and showed in Chapter 3.3.3, is displayed and compared to the maxima predicted by the model. The relative error is also showed.

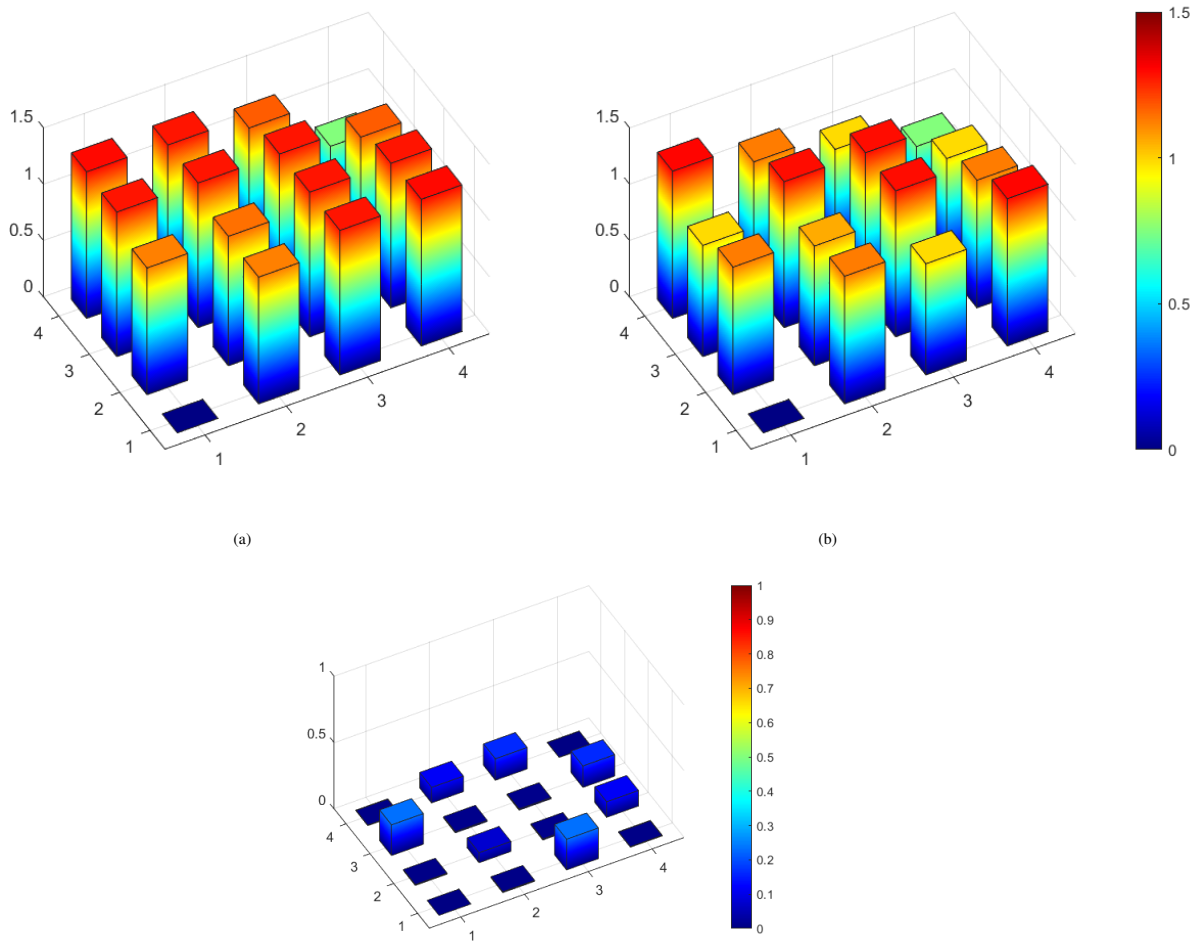


Figure 5.11: (a) Real maximum relative overload reached in the entire network plotted against the location of the closing valve node. (b) Prediction of the model of such metric. (c) Relative error made by the model.

This metric shows how the predictive model fails to grasp the dangerousness, intended as the capability of generating local peaks of overpressure, closing valves on the border nodes far from the reservoir.

In Figure 5.12 the metric that associates each node to the mean of the maximum relative overloads reached on every node after the closing of its valve, described and showed in Chapter 3.3.2, is displayed and compared to the mean of the maxima predicted by the model. The relative error is also showed.

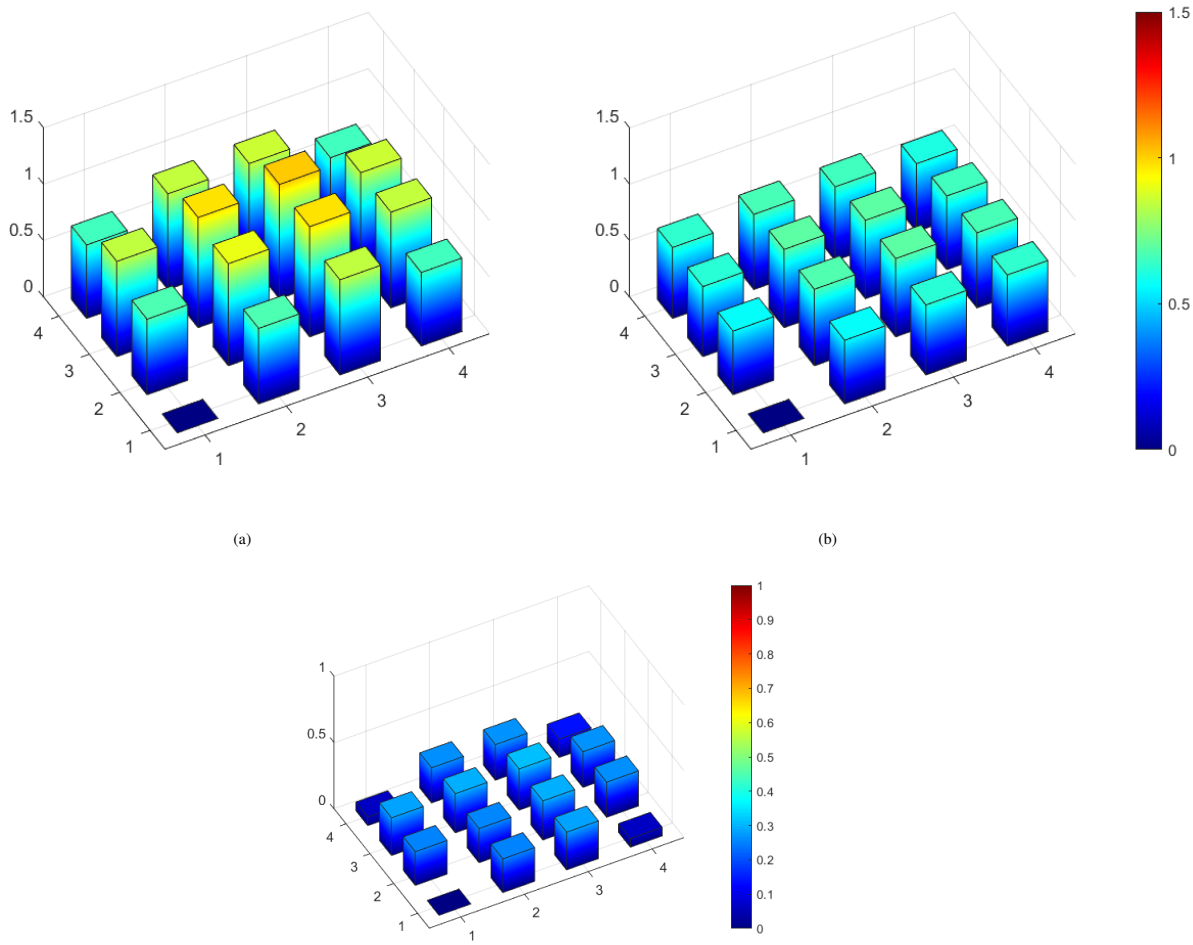


Figure 5.12: (a) Real spatial mean of the maximum relative overloads reached in the entire network plotted against the location of the closing valve node. (b) Prediction of the model of such metric. (c) Relative error made by the model.

This metric shows how the predictive model fails to grasp the dangerousness, intended as the capability of generating a high-peaked global average overpressure, of closing valves on almost every node, except for the vertices, in particular the two not opposite to the reservoir.

# CONCLUSIONS

In this work of thesis, a preliminary study of pressure waves propagation has been carried out on square lattice hydraulic networks of different sizes, with a reservoir on a vertex and valves on every other node. Computer simulations have been carried out, closing abruptly the valve on a node and letting the pressure and velocity waves propagate through the network. The simulation data have been elaborated and condensed into significant metrics, such as the maximum overload reached in the entire network or the spatial mean of the temporal maxima reached on the different nodes, to characterize each node with the effects closing its valve would have on the entire network. We observed a strong non-locality of the phenomenon and peaks of overpressure even higher than that originated at the closing of the valve. A better understanding of the propagating mechanism of pressure and velocity waves inside networks at multi-conduits junctions was necessary. Starting from a simplification of the characteristic equations, we derived a toy model for the propagation of pressure waves along *direct paths*. We found the prediction of the overloads reached at the first arrival of the pressure waves to be precise, so we also improved it to account for dissipation effects. We carried out an analysis to find out the statistics of *max-first connections* and the average delay of maxima with respect to the first arrival of the waves. We found out that the fraction of max-first connection between nodes with a low number of nearest neighbors is greater than that of connections between nodes with higher number of nearest neighbors. The values of these fractions are either stable or slightly decreasing with the enlarging of the network, after a first adjustment for small networks. From these analysis, we expected the toy model to work better for nodes with a smaller number of nearest neighbours, when trying to predict the real maximum overload with the first overload computed with the model. Then, we tried to use prediction on the first overloads for estimating the maximum overloads on the network with  $n = 3$  conduits per size. The maximum overload metric is exactly reconstructed for 2- $nn$  and 4- $nn$  nodes (except for a little error on node 6) and the spatial mean of temporal maxima metrics is only predicted for 2- $nn$  nodes.

Further studies are required for a deeper comprehension of the power of prediction of this model as a function of different topologies of the network it is applied to. Furthermore, more studies on wave propagation through *non-direct* paths and their possible modelization will be useful to improve predictions based on new network approaches.

# Bibliography

- [1] M. H. Chaundry. Applied Hydraulics Transients. New York, NY: Van Nostram Reinhold company, 1979, pp. 2–61.
- [2] I. Newton. The Principia. Book 2, Proposition 44-46. London: Royal Soc., 1687.
- [3] L. Euler. “De la Propagation du Son”. In: Mémoires de l’Acad. d. Wiss. (1759).
- [4] L. Euler. Principia pro Motu Sanguinis per Arterias Determinando. Opera Postume Tomus Alter, XXXIII. 1775.
- [5] I. L. Lagrange. Mequanique analitique, p. 192. Bertrand’s ed. Paris, 1778.
- [6] P. S. Laplace. Celestial Mechanics. 4 volumes, Bowditch translation.
- [7] T. Young. Hydraulic Investigations. London, 1808.
- [8] M. Marey. “Mouvement des Ondes Liquides pour Servir a la Theoire du Pouls”. In: Travaux du Laboratoire de M. Marey (1875).
- [9] D. J. Korteweg. “Ueber die Fortpflanzungsgeschwindigkeit des Schalles in elastischen Rohren”. In: Annalen der Physik und Chemie 5.12 (), pp. 525–542.
- [10] J. Michaud. “Coups de béliet dans les conduites, étude des moyens employées pour en ateneur les effets”. In: Bulletin de la Société Vaudoise des Ingénieurs et des Architectes 4.3 and 4 (1878), pp. 56–64, 65–77.
- [11] L. F. Menabrea. “Note sur les effects de choc de l’eau dans le conduites”. In: Comptes Rendus Hebdomadaires des Séances de L’Academie des Sciences 47.July-Dec. (1858), pp. 221–224.
- [12] I. S. Gromeka. “Concerning the Propagation Velocity of Waterhammer Waves in Elastic Pipes”. In: Scientific Soc. of Univ. of Kazan (May 1883).
- [13] J. P. Frizell. “Pressure Resulting from Changes of velocity of Water Pipes”. In: Trans. Amer. Soc. Civil Engrs. 39 (June 1898), pp. 1–18.

- [14] N. E. Joukovski. Mem. Imperial Acadamey Soc. of St. Petersburg. Vol. 9. 5. 1898.
- [15] E. B. Weston. “Description of Some Experiments Made on the Providence, R. I. Water Works to Ascertain the Force of Water Ram in Pipes”. In: Trans. Amer. Soc. of Civil Engrs. 14 (1885).
- [16] R. C. Weston. “Experiments on Waterhammer”. In: Trans. Amer. Soc. of Mech. Engrs. (1893-1894).
- [17] L. Allievi. “Teoria generale del moto perturbato dell’acqua nei tubi in pressione”. In: Ann. Soc. Ing. Arch. italiana (1903).
- [18] C. Lai. “A study of Waterhammer Including Effect of Hydraulic Losses”. In: Thesis presented to the University of Michigan (1962).
- [19] Streeter V. L. and C. Lai. “Waterhammer Analysis Including Fluid Friction”. In: Trans. Amer. Soc. Civ. Engrs 128 (), pp. 1491–1524.
- [20] G. Monge. “Graphical Integration”. In: Ann. des Ing. Sortis des Ecoles de Gand (1789).